Neutrino Flavor Conversions in Dense Media

by

Lei Ma

Supervisor:
Professor Huaiyu Duan

Doctor of Philosophy in Physics, University of New Mexico, 2018

Abstract

One of the interesting and important problems in astrophysics is the mechanism of core-collapse supernova explosions. Many numerical simulations have shown that the explosion shock would stall. Different proposals have been made to explain the core-collapse supernovae, among which the neutrino mechanism is promising and most researched one. To explore the mechanism, prediction of the neutrino flavors in core-collapse supernovae is crucial. Neutrino flavor conversions are altered by the matter, neutrinos themselves, as well as other factors such as the geometries of the neutrino emissions. The complexity of the problem requires breaking it down into investigations of each simple yet specific situation.

Neutrinos propagating through a matter background experience a potential which changes the flavor conversions. One of the important mechanisms is the Mikheyev–Smirnov–Wolfenstein effect. However, much more complicated density profiles of matter, such as periodic density profiles, may lead to large flavor conversion, which is dubbed as stimulated oscillations by J. Kneller et al. Mathematics of such large conversion has been established but without clear pictures. For the two-flavor scenario, neutrino oscillations is a two-level quantum system, and it reminds us of many two-level quantum problems that have been solved in the past. We draw analogies between neutrinos passing through matter and Rabi oscillations in optics, which allows us to calculate resonance conditions and flavor survival probability easily.

As for neutrinos flavors with high number densities, nonlinear interactions come into play since neutrino forward scattering provides another potential that is related to the flavor of the neutrinos themselves. Nonlinearity makes the flavor conversion hard to predict by intuition. The treatment is linearizing the equation of motion and identifying instabilities. One of the tricks in the realm is to utilize the dispersion relation. In principle, dispersion relations tell us how waves propagate for different wave numbers and frequencies. However, the neutrino problem is much more complicated. Situations that are inconsistent with the dispersion relation approach are identified.

Finally, forward scattering of supernova neutrinos are not the only thing that happens. During propagation around a supernova, neutrinos may be scattered in every direction, which forms a neutrino halo. The halo couples the neutrinos nonlocally, which then becomes a nonlocal boundary value problem. One of the solutions is the relaxation method. Starting from some state of neutrinos and relaxing the system into equilibrium has proven to be a working algorithm. A numerical algorithm is developed and neutrino line model with back scattering is investigated.

Chapter 1

Introduction

1.1 The Little Neutral One

The neutrino has been one of the most interesting particles that has ever been discovered. Its fanscinating history started with the observation of beta decay, i.e., the emission of electrons in nuclear decays, such as

$$^{14}_{6}\mathrm{C} \rightarrow ^{17}_{7}\mathrm{N} + \mathrm{e}^{-} + \bar{\nu}_{\mathrm{e}}.$$

The fact that the electron energy spectrum in the beta decay process is continuous indicates the existence of a third product other than $^{17}_{7}\mathrm{N}$ and e^{-}. In 1930, Pauli wrote a letter to a workshop in Tubingen explaining to the "Radioactive Ladies and Gentlemen" about his so called "neutron" as the missing particle in beta decay at that time. It was then called the neutrino since the name "neutron" was latter used to name one of the nucleons. The missing particle $\bar{\nu}_{\mathrm{e}}$ in beta decays was then proven to be the anti-neutrino. In nuclear beta decays, the charged current weak interaction converts a down quark in the neutron to an up quark while releasing an electron and an anti-electron neutrino,

$$n \rightarrow p + e^{-} + \bar{\nu}_{e}. \tag{1.1}$$

More generally, the positron/electron emission and capture processes are all neutrino-related nuclear reactions which are listed in Table 1.1. There are three different flavors of neutrinos, namely the electron flavor, the muon flavor, and the tau flavor as shown in Table 1.2. The first direct detection of neutrinos was done by Clyde Cowan and Frederick Reines in 1956 [1] who used nuclear reactor neutrinos as the source of the experiment.

Reaction Type	Process	Mediator(s)
Electron emission	${}^{A}_{Z}X \rightarrow {}^{A}_{Z+1}X' + e^- + \bar{\nu}_e$	$W^{\pm}$
Positron emission	${}^{A}_{Z}X \rightarrow {}^{A}_{Z-1}X' + e^+ + \nu_e$	$W^{\pm}$
Electron capture	${}^{A}_{Z}X + e^- \rightarrow {}^{A}_{Z-1}X' + \nu_e$	$W^{\pm}$
Positron capture	${}^{A}_{Z}X + e^+ \rightarrow {}^{A}_{Z+1}X' + \bar{\nu}_e$	$W^{\pm}$
$e^{\pm}$ annihilation	$e^- + e^+ \rightarrow \nu + \bar{\nu}$	$W^{\pm}$, Z
Bremsstrahlung	$X + X' \rightarrow X + X' + \nu + \bar{\nu}$	Z
$\nu(\bar{\nu})$ capture	${}^{A}_{Z}X + \overset{(-)}{\nu}_e \rightarrow {}^{A}_{Z\mp1}X' + e^{\pm}$	$W^{\pm}$
$e^{\pm}\nu$ scattering	$e^- + \overset{(-)}{\nu} \rightarrow e^- + \overset{(-)}{\nu}$	$W^{\pm}$, Z
Nucleon scattering	${}^{A}_{Z}X + \overset{(-)}{\nu} \rightarrow {}^{A}_{Z}X + \overset{(-)}{\nu}$	Z

Table 1.1: Neutrino related nuclear and leptonic reactions.

[0.5ex] Electric Charge	0
Spin	1/2
Mass	< 2 eV
Interactions	Weak, Gravitation
Flavors	ν_e, ν_μ, ν_τ
Chirality	Left
Hypercharge	-1

Table 1.2: The physical properties of the neutrino [35].

1.2 Stellar Neutrinos

Besides man-made sources, neutrinos are also produced in many astrophysical environments.For example, numerous nuclear reactions occur in stellar cores which produce luminous neutrino fluxes. The most important nuclear reactions in the Sun are the pp chain reactions which are shown in Fig. 1.1. In order to calculate the neutrino spectrum we need the neutrino production rate in each reaction and the branching ratios. Solar neutrinos are mostly produced in the pp reaction, Be electron capture and B decay which are labeled in red in Fig 1.1:

$$\begin{aligned} &\mathrm{p} + \mathrm{p} \rightarrow {}^{2}\mathrm{H} + \mathrm{e}^{+} + \nu_{\mathrm{e}} && \leq 0.422\mathrm{MeV}, \\ &{}^{7}\mathrm{Be} + \mathrm{e}^{-} \rightarrow {}^{7}\mathrm{Li} + \nu_{\mathrm{e}} && 0.862\mathrm{MeV\ for\ 90\%}, \\ & && 0.384\mathrm{MeV\ for\ 10\%}, \\ &{}^{8}\mathrm{B} \rightarrow {}^{8}\mathrm{Be}^{*} + \mathrm{e}^{+} + \nu_{\mathrm{e}} && \leq 15\mathrm{MeV}. \end{aligned}$$

Even without the knowledge of the detailed reactions, the conservation of the electric charge and the electron lepton number will lead to the overall neutrino production formula

$$4\mathrm{p} + 2\mathrm{e}^{-} \rightarrow {}^{4}\mathrm{He} + 2\nu_{\mathrm{e}}. \tag{1.2}$$

It is important to notice that two neutrinos are emitted for each α particle, i.e., ^{4}He, produced in the Sun. Using this simple relation, we can estimate the neutrino number flux emitted by the Sun. The energy released during the production of each α particle is the difference between the initial and final rest masses of the particles,

$$Q = 4m_p + 2m_e - m_\alpha = 26.7\mathrm{MeV}, \tag{1.3}$$

where the mass of the neutrinos are neglected. On average, each neutrino carries away an energy of 0.2MeV and the rest of the energy is in the form of thermal energy $Q_\gamma = 26.3$MeV [23]. Since two neutrinos are emitted for the production of thermal

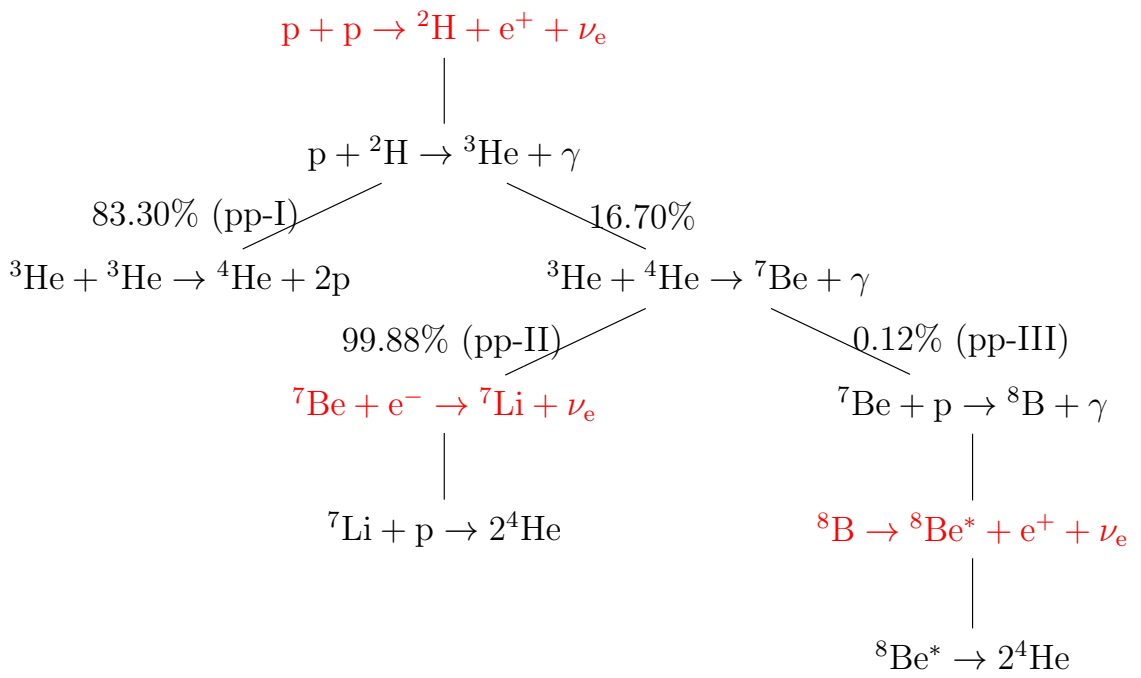

Figure 1.1: The pp chain reactions with the corresponding branching ratios. The branching ratios are taken from Ref. [12].

energy Q_γ, the number flux of the solar neutrinos near the Earth is approximately

$$\Phi_\nu = \frac{2S_0}{Q_\gamma} \approx 6 \times 10^{10} \mathrm{cm}^{-2}\mathrm{s}^{-1}, \tag{1.4}$$

where the solar constant S_0 is the energy flux of solar photons on the top of the Eath atmosphere.

As the detection of neutrinos became feasible, Ray Davis and John Bahcall et al worked out the solar neutrino flux and led the Homestake experiment to measure the solar neutrinos. The results revealed that the neutrino flux detected was less than what was predicted by the standard solar model [3]. This is the solar neutrino problem. It is now known that the solution to the problem is related to the neutrino. The electron neutrinos produced in the solar core transform to other flavors while they travel to the Earth. This phonomenon is referred known as the flavor transformation of the neutrino, or neutrino oscillations. The theory of neutrino oscillations

was first proposed by Pontecorvo in 1968 [2]. The field of neutrino oscillations has grown significantly into a broad field in physics since then.

1.3 Supernova Neutrinos

Another astronomical source of neutrinos is the core-collapse supernova explosion. Massive stars with masses larger than 6−8 solar masses are very bright. However, violent delights have violent ends. When the core of a massive star runs out of nuclear fuel, it collapses under it's own gravity. During the collapse, the inner core is compressed to almost nuclear density, which has a stiff equation of state. The materials falling onto the highly compressed inner core are bounced outward which generates a shock wave and may lead to an explosion. However, supernova simulations to date show that the shock wave itself is not always energetic enough to produce the explosion [34]. In most cases, it stalls and becomes a standing accretion shock wave. To revive the shock, more energy has to be deposited behind the shock. A possible solution is to introduce reheating of the shock by neutrinos [34]. In fact 99% percent the energy released in a core-collapse supernova is carried away by neutrinos. In order to implement the neutrino-driven mechanism in computer simulations of supernovae, the flux and flavor content of the neutrinos have to be known everywhere behind the shock. Thus neutrino oscillations in dense matter become a key to the supernova explosion problem.

The average energy of the neutrinos $\langle E \rangle$ emitted during a supernova explosion is of the order of 10MeV [40], and the neutrino luminosity at the early epoch is approximately $10^{52}\text{ergs} \cdot \text{s}^{-1}$ [24]. Therefore, the number density of the neutrinos at the radius R is

$$n \sim 10^{18}\text{cm}^{-3} \left(\frac{100\text{km}}{R}\right)^2 \left(\frac{10\text{MeV}}{\langle E \rangle}\right).$$

It turns out that the ambient dense neutrino medium has a significant impact on

neutrino oscillations, which has been intensely investigated in the last decade [21].

Observation-wise, the neutrino signals from a galactic supernova can reveal a great amount of information about the physical conditions inside the supernova. In fact, the detection of supernova neutrinos is on the task list of the Deep Underground Neutrino Experiment (DUNE) [41].

1.4 Organization of the Disseration

The rest of the disseration is organized as follows. In Chapter 2, I will review neutrino oscillations in vacuum and in environments with smooth matter density profiles. In Chapter 3, I will discuss my work on neutrino oscillations in oscillatory matter profiles, which can be decomposed into Fourier modes and interpreted as a superposition of Rabi oscillations. In Chapter 4, I will first review how neutrino self-interactions can cause a dense neutrino medium to oscillate collectively. Then I will discuss my study on the dispersion relations of the collective modes of neutrino oscillations. I will also discuss a premilinary work on neutrino oscillations when both forward and backward neutrino fluxes are present. In Chapter 5, I will summarize my work and discuss possible future directions of the field.

Chapter 2

General Principles of Neutrino Oscillations

Because the flavor eigenstates of the neutrino are not the same as its propagation eigenstates, it can change flavor while it propagates. In this chapter, I will use the two-flavor scheme to explain neutrino oscillations in some simple scenarios[1]. I will first discuss neutrino oscillations in vacuum. After explaining the general principles of neutrino oscillations in matter, I will show how the solar neutrino problem can be explained by neutrino oscillations. Finally, I will demonstrate the flavor isospin picture which can be used to visualize neutrino oscillations.

[1]In most physical problems, the two-flavor scheme is a good approximation to the phenomena of neutrino oscillations. The mass splits between the three mass eigenstates are so different that the corresponding oscillations occur on very different length scales. On the right length scale, the two-flavor scheme captures the prominent features of the neutrino oscillations of the corresponding mass split.

2.1 Vacuum Oscillations

Before working out the math, I can estimate the frequency of the oscillations of the neutrino between its flavors. In the natural units, frequency has the same dimension as energy (see Appendix **??**). Consider an electron neutrino with momentum p which is a superposition of the two mass eigenstates $|\nu_i\rangle$ $(i = 1, 2)$ with masses m_i, respectively. Since the neutrino masses are small, I can Taylor expand the energy of each mass eigenstate in terms of the corresponding mass:

$$\begin{aligned} E_i &= \sqrt{m_i^2 + p^2} \\ &= p\sqrt{\frac{m_i^2}{p^2} + 1} \\ &\approx p + \frac{1}{2}\frac{m_i^2}{p}. \end{aligned} \tag{2.1}$$

The first term in the above equation produces a global phase to the flavor wave function of the neutrino which does not affect neutrino flavor oscillations. The characteristic energy scale in the problem is the difference between the energies of the two mass eigenstates,

$$\omega_{\mathrm{v}} = \frac{m_2^2 - m_1^2}{2E} = \frac{\delta m^2}{2E}, \tag{2.2}$$

which turns out to be the vacuum oscillation frequency. Here $E = p$ is approximately the energy of the neutrino.

To work out the exact solution, I will utilize the Schrödinger equation. The wave function in flavor basis $\Psi^{(\mathrm{f})}$ is related to the wave function in mass basis $\Psi^{(\mathrm{v})}$ through a unitary mixing matrix U,

$$\Psi^{(\mathrm{f})} = \mathsf{U}\Psi^{(\mathrm{v})}, \tag{2.3}$$

where the upper indices $^{(\mathrm{v})}$ and $^{(\mathrm{f})}$ are used to denote the corresponding bases. The

mixing matrix can be expressed using the vacuum mixing angle $\theta_{\rm v}$,

$$\mathsf{U} = \begin{pmatrix} \cos\theta_{\rm v} & \sin\theta_{\rm v} \\ -\sin\theta_{\rm v} & \cos\theta_{\rm v} \end{pmatrix}. \tag{2.4}$$

In vacuum mass basis, the neutrino has a free propagation Hamiltonian

$$\mathsf{H}^{(\rm v)} = \begin{pmatrix} E_1 & 0 \\ 0 & E_2 \end{pmatrix}. \tag{2.5}$$

To the first order, the Hamiltonian becomes

$$\begin{aligned} \mathsf{H}^{(\rm v)} &\approx \frac{1}{2E}\begin{pmatrix} m_1^2 & 0 \\ 0 & m_2^2 \end{pmatrix} + E\mathsf{I} \\ &= \frac{1}{4E}\begin{pmatrix} -\delta m^2 & 0 \\ 0 & \delta m^2 \end{pmatrix} + \left(\frac{m_2^2+m_1^2}{4E} + E\right)\mathsf{I}. \end{aligned} \tag{2.6}$$

Because a multiple of the identity matrix I only gives an global phase to the neutrino flavor wave function, I will neglect it from now on, and the vacuum Hamiltonian simplifies to

$$\mathsf{H}^{(\rm v)} = \frac{\delta m^2}{4E}\begin{pmatrix} -1 & 0 \\ 0 & 1 \end{pmatrix} = -\frac{\delta m^2}{4E}\sigma_3 = -\frac{\omega_{\rm v}}{2}\sigma_3, \tag{2.7}$$

where

$$\sigma_1 = \begin{pmatrix} 0 & 1 \\ 1 & 0 \end{pmatrix}, \qquad \sigma_2 = \begin{pmatrix} 0 & -\mathrm{i} \\ \mathrm{i} & 0 \end{pmatrix}, \qquad \sigma_3 = \begin{pmatrix} 1 & 0 \\ 0 & -1 \end{pmatrix} \tag{2.8}$$

are the three Pauli matrices. The Schrödinger equation has the following simple solution in mass basis:

$$\Psi^{(\rm v)}(t) = \begin{pmatrix} c_1(0)e^{i\omega_{\rm v}t/2} \\ c_2(0)e^{-i\omega_{\rm v}t/2} \end{pmatrix}. \tag{2.9}$$

Using Eqn. 2.3, I obtain the wave function in flavor basis,

$$\Psi^{(\rm f)}(t) = \mathsf{U}\Psi^{(\rm v)}(t) \tag{2.10}$$

$$= \begin{pmatrix} \cos\theta_{\rm v} & \sin\theta_{\rm v} \\ -\sin\theta_{\rm v} & \cos\theta_{\rm v} \end{pmatrix}\begin{pmatrix} c_1(0)e^{i\omega_{\rm v}t/2} \\ c_2(0)e^{-i\omega_{\rm v}t/2} \end{pmatrix}. \tag{2.11}$$

Alternatively, I can also determine the Hamiltonian in flavor basis first, which is

$$\mathsf{H}^{(\mathrm{f})} = \mathsf{U}\mathsf{H}^{(\mathrm{v})}\mathsf{U}^{\dagger} = -\frac{\omega_{\mathrm{v}}}{2}\cos 2\theta_{\mathrm{v}}\sigma_3 + \frac{\omega_{\mathrm{v}}}{2}\sin 2\theta_{\mathrm{v}}\sigma_1. \tag{2.12}$$

By solving the Schrödinger equation in flavor basis, I will obtain the same wave function as in Eqn. 2.11.

The probability for a neutrino emitted in the electron flavor at time $t = 0$ to be detected as the electron flavor at a later time t is

$$P(t) = 1 - \sin^2(2\theta_{\mathrm{v}})\sin^2\left(\frac{\omega_{\mathrm{v}}t}{2}\right). \tag{2.13}$$

Since the neutrino travels with approximately the speed of light, the electron neutrino survival probability at a distance r from the source is

$$P(r) = 1 - \sin^2(2\theta_{\mathrm{v}})\sin^2\left(\frac{\omega_{\mathrm{v}}}{2}r\right). \tag{2.14}$$

I plot the above result in Fig. 2.1 which clearly shows the oscillatory behavior. The oscillation length is determined by the characteristic energy scale ω_{v}, which confirms our qualitative method result in Eqn. 2.2. The oscillation amplitude is determined by $\sin^2(2\theta_{\mathrm{v}})$.

In nature, there are three neutrino flavors and, correspondingly, three neutrino mass eigenstates, which are shown in Fig. 2.2. Because there are two different characteristic energy scales, $\omega_{\mathrm{v},21} = \delta m^2_{21}/2E$ and $\omega_{\mathrm{v},32} = \delta m^2_{31}/2E$, two oscillation periods should occur, as shown in Fig. 2.3. The fast oscillations are determined by the larger energy scale, $\omega_{\mathrm{v},32}$, while the slow oscillations are determined by the smaller one $\omega_{\mathrm{v},21}$. For the inverted neutrino mass hierarchy (with $m_3 < m_1 < m_2$), the oscillation frequencies are the same as in the normal mass hierarchy (with $m_3 > m_2 > m_1$) since they have the same characteristic energy scales. However, they will develop different phases during oscillations.

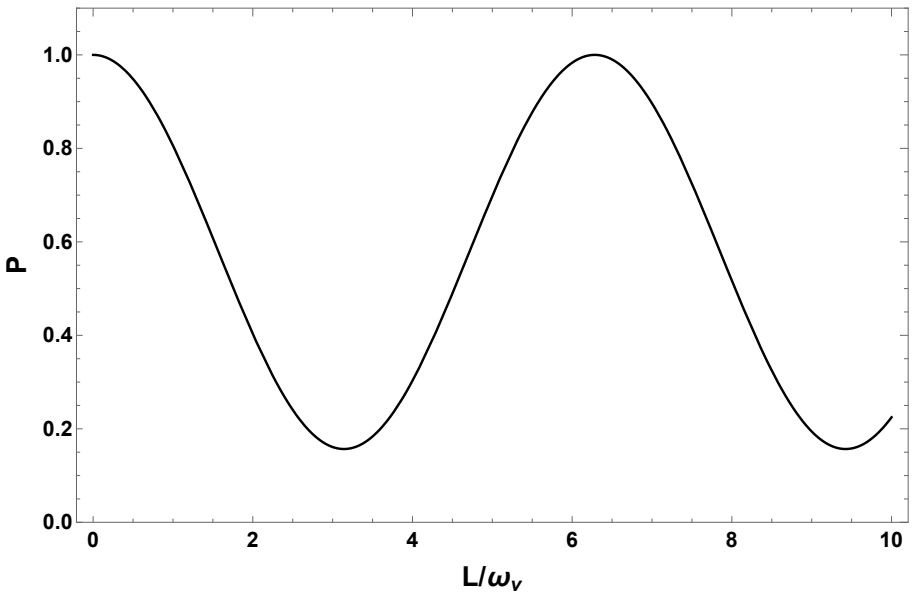

Figure 2.1: The electron flavor neutrino survival probability in vacuum oscillations as a function of distance r which is measured in terms of vacuum oscillation frequency ω_{v}. The mixing angle θ_{v} is given by $\sin^2\theta_{\mathrm{v}} = 0.30 \approx \sin^2\theta_{12}$.

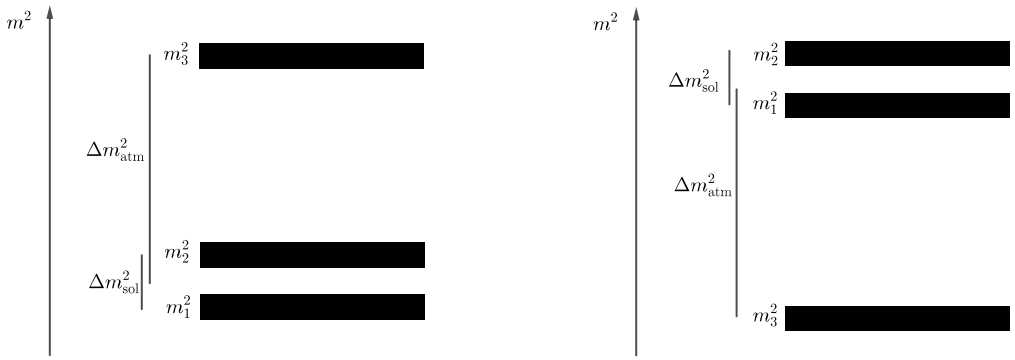

(a) Normal hierarchy: the third mass is heavier than the first two.

(b) Inverted hierarchy: the third mass is smaller than the first two.

Figure 2.2: The order of the three neutrino masses. The difference between the first two masses is responsible for solar neutrino oscillations, and the difference between the third mass and the first two is responsible for atmospheric neutrino oscillations.

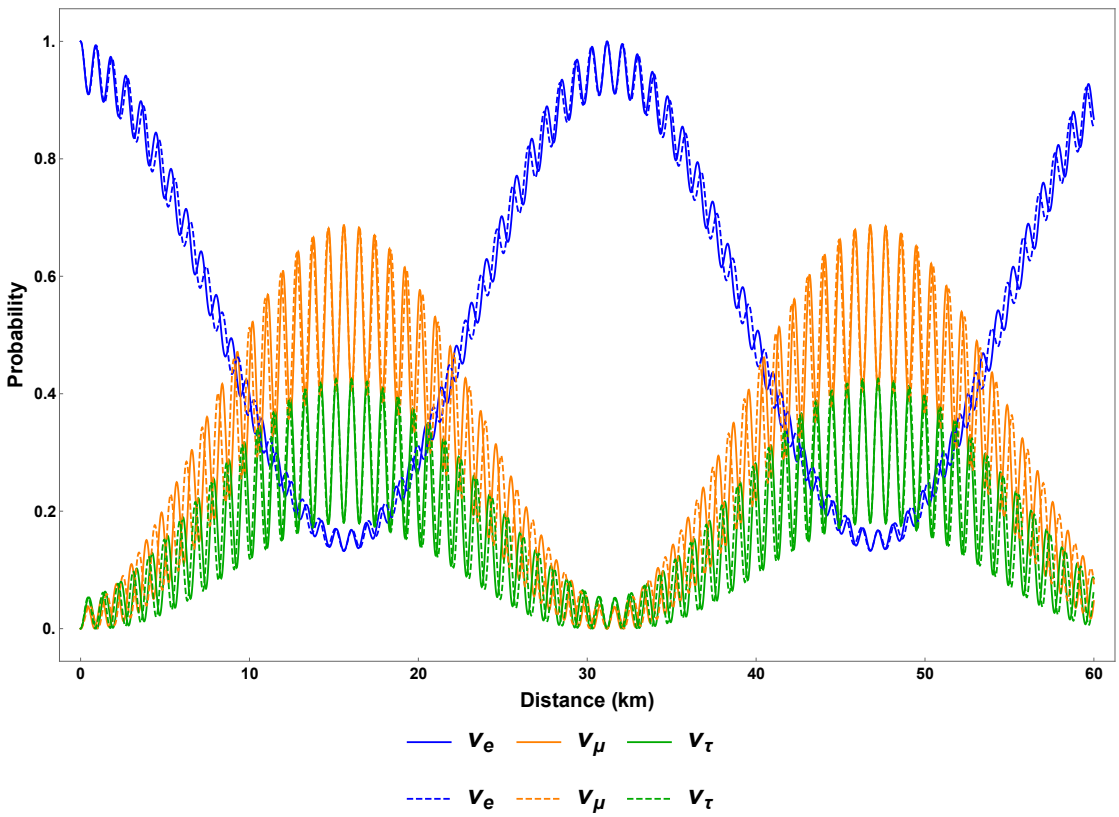

Figure 2.3: The probabilities for a 1MeV neutrino, which is in the electron flavor initially, in different flavors as functions of the distance in vacuum. The solid lines represent the normal hierarchy and the dashed lines represent the inverted hierarchy. The mixing angles are $\sin^2\theta_{12} = 0.30$, $\sin^2\theta_{13} = 0.023$, and $\sin^2\theta_{23} = 0.41$, respectively, and the mass differences are $\delta m^2_{21} = 7.9 \times 10^{-5}\text{eV}^2$ and $\delta m^2_{23} = 2.7 \times 10^{-3}\text{eV}^2$.

2.2 Neutrino Oscillations in Matter

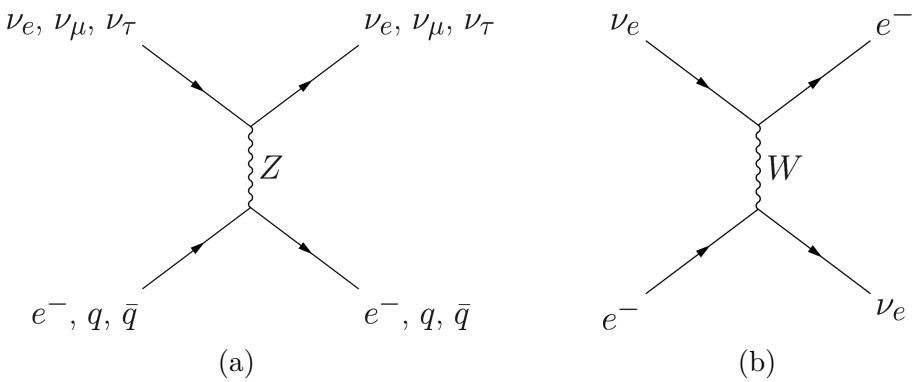

Figure 2.4: (a) The neutral current weak interaction does not distinguish between neutrino flavors and has no impact on neutrino oscillations. (b) The electron flavor neutrino acquires a unique refractive index contribution from the charged current weak interaction with ambient electrons.

In many astrophysical environments, such as stars and core-collapse supernovae, neutrinos are mostly produced at the center of the object and propagate through the dense matter envelope. Although this matter envelope is essentially transparent to neutrinos, the refractive indices of the neutrinos in matter are different than those in vacuum.[2] Because the neutral current weak interaction does not distinguish between neutrino flavors (see Fig. 2.4a), it has no impact on neutrino oscillations, and I will ignore it from now on. Meanwhile, the electrons and positrons in matter will cause electron flavor neutrinos to have refractive indices different than other neutrino flavors through the charged current weak interaction (see Fig. 2.4b). This leads to an effective potential

$$\mathsf{V}^{(\mathrm{f})} = \frac{\sqrt{2} G_{\mathrm{F}} n_{\mathrm{e}}}{2} \sigma_3, \tag{2.15}$$

where G_{F} is Fermi constant and n_{e} is net number density of the electron. As usual,

[2]The word "matter" in this disseration refers to ordinary matter composed of electrons, positrons, nucleons and nuclei. We assume that the temperature and density of the environment are not high enough to produce muons and tau particles. We will discuss the effect of dense neutrino medium in Chapter 4.

I have ignored the trace terms in the above equation.

The Hamiltonian with the matter effect is the combination of Eqn. 2.12 and Eqn. 2.15:

$$\mathsf{H}^{(\mathrm{f})} = \left(\frac{\lambda}{2} - \frac{\omega_{\mathrm{v}}}{2} \cos 2\theta_{\mathrm{v}} \right) \sigma_3 + \frac{\omega_{\mathrm{v}}}{2} \sin 2\theta_{\mathrm{v}} \sigma_1, \tag{2.16}$$

where

$$\lambda = \sqrt{2} G_{\mathrm{F}} n_{\mathrm{e}}. \tag{2.17}$$

Due to the off-diagonal terms in $\mathsf{H}^{(\mathrm{f})}$, the neutrino will experience oscillations in flavor. A resonance with the maximum flavor mixing occurs when the diagonal terms of $\mathsf{H}^{(\mathrm{f})}$ vanish,

$$\frac{\lambda}{2} - \frac{\omega}{2} \cos 2\theta_{\mathrm{v}} = 0, \tag{2.18}$$

which gives the Mikheyev–Smirnov–Wolfenstein (MSW) resonance condition.

2.3 Neutrino Oscillations in the Sun

The neutrinos produced in the solar core experience decreasing matter density as they travel outward through the Sun. The neutrino propagation eigenstates are different from the flavor states in general [5]. Because the density change inside the Sun is not dramatic, the flavor quantum states of the neutrinos will evolve adiabatically inside the Sun.

The values of the instantaneous eigenstates of the Hamiltonian, known as the heavy and light states, are

$$\varepsilon_{\mathrm{H}} = \frac{\omega_{\mathrm{v}}}{2} \sqrt{\hat{\lambda} + 1 - 2\hat{\lambda} \cos 2\theta_{\mathrm{v}}}, \tag{2.19}$$

$$\varepsilon_{\mathrm{L}} = -\frac{\omega_{\mathrm{v}}}{2} \sqrt{\hat{\lambda} + 1 - 2\hat{\lambda} \cos 2\theta_{\mathrm{v}}}, \tag{2.20}$$

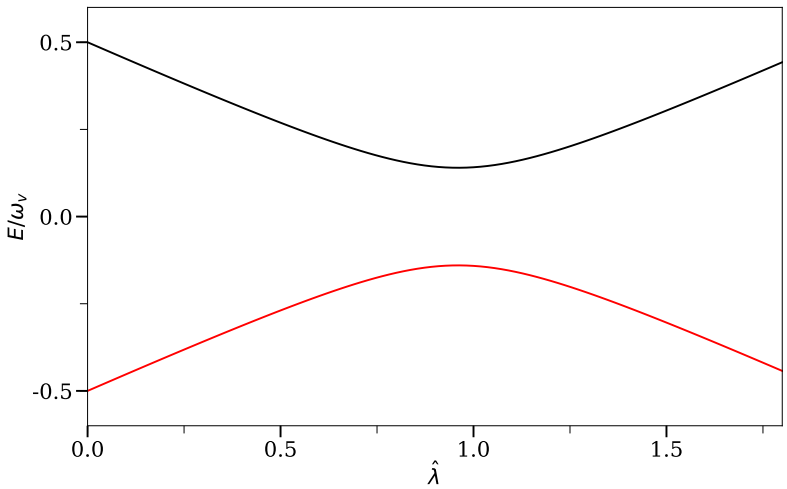

Figure 2.5: The two eigenvalues of the neutrino Hamiltonian as functions of matter potential $\hat{\lambda}$. I have used $\sin^2\theta_{\rm v} = 0.02 \approx \sin^2\theta_{13}$.

where

$$\hat{\lambda} = \frac{\lambda}{\omega_{\rm v}}. \tag{2.21}$$

In Fig. 2.5, I show the two eigenvalues of the neutrino Hamiltonian as functions of the matter potential $\hat{\lambda}$.

For a very high matter density, the heavy state of the neutrino $|\nu_{\rm H}\rangle$ is almost the same as $|\nu_{\rm e}\rangle$. As the matter density decreases, $|\nu_{\rm H}\rangle$ becomes a mixture of different neutrino flavors. As the neutrino reaches the surface of the Sun, where the matter density is approximately zero, $|\nu_{\rm H}\rangle$ is about the same as vacuum mass eigenstate $|\nu_2\rangle$. As a result, the electron flavor neutrinos produced at the solar core are partially converted to other flavors as they reach the surface of the Sun. This explains the solar neutrino problem.

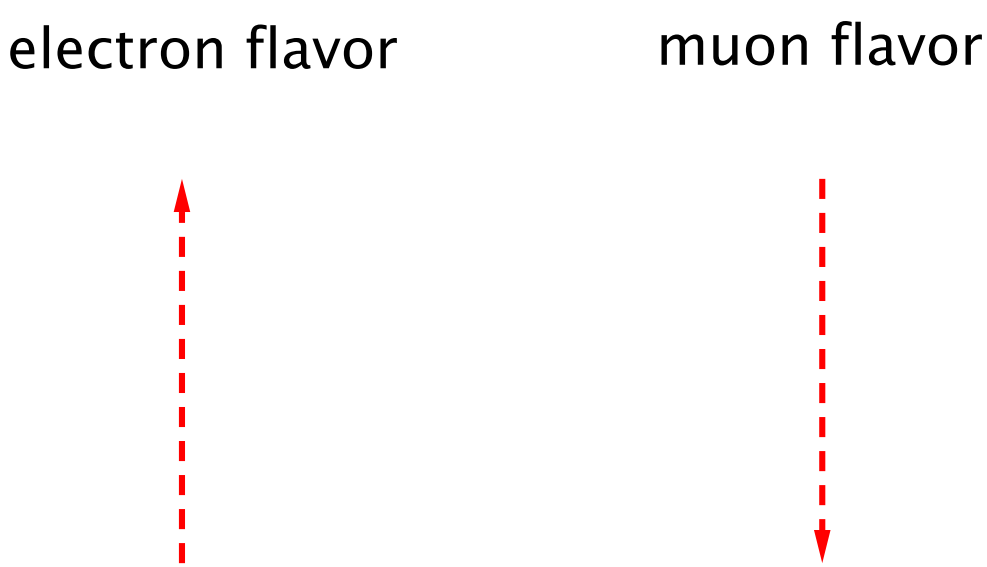

Figure 2.6: In the flavor isospin picture, a flavor isospin pointing upward, i.e., along the third axis in flavor space, indicates that the neutrino is in the electron flavor, while the downward direction indicates the other flavor, such as the muon flavor.

2.4 Flavor Isospin Formalism

The Hamiltonian for two-flavor neutrino oscillations describes a two-level quantum system. It is known that two-level quantum systems can be visualized using the Bloch sphere. In the realm of neutrino physics, the neutrino flavor isospin was introduced for such purpose [15].

Every two-by-two Hermitian matrix can be expanded in the quaternian basis. For example, the Hamiltonian for neutrino oscillations in vacuum (in flavor basis) can be written as

$$\mathsf{H}^{(\mathrm{f})} = -\frac{\vec{\sigma}}{2} \cdot \vec{H}, \tag{2.22}$$

where

$$\vec{H} = \omega_{\rm v} \begin{pmatrix} \sin\theta_{\rm v} \\ 0 \\ \cos 2\theta_{\rm v} \end{pmatrix},$$

which is a vector of length $\omega_{\rm v}$ and tilted away from the third axis by the angle $2\theta_{\rm v}$. Throughout the dissertation, I will use " $\vec{}$ " to denote a vector in flavor space. The flavor quantum state of the neutrino is represented by the flavor isospin, which is defined as

$$\vec{s} = \Psi^{(\rm f)\dagger} \frac{\vec{\sigma}}{2} \Psi^{(\rm f)}. \tag{2.23}$$

As shown in Fig. 2.6, the direction of the flavor isospin in flavor space shows the flavor content of the neutrino. A flavor isospin pointing upward in flavor space, i.e., along the direction of the third axis, denotes the electron flavor by definition. Correspondingly, the equation of motion for the flavor isospin describes its precession around the vector $\vec{H}$,

$$\dot{\vec{s}} = \vec{s} \times \vec{H}. \tag{2.24}$$

In the flavor isospin formalism, the electron flavor survival probability is

$$P = \frac{1}{2} + s_3,$$

where s_3 is the third component of the flavor isospin. Therefore, the precession of the flavor isospin corresponds to a periodic oscillation between the two neutrino flavors (see Fig. 2.7). The oscillation frequency is trivially read out from Eqn. 2.24,

$$\omega_{\rm v} = |\vec{H}|. \tag{2.25}$$

The MSW effect can also be easily explained using the flavor isospin picture. The

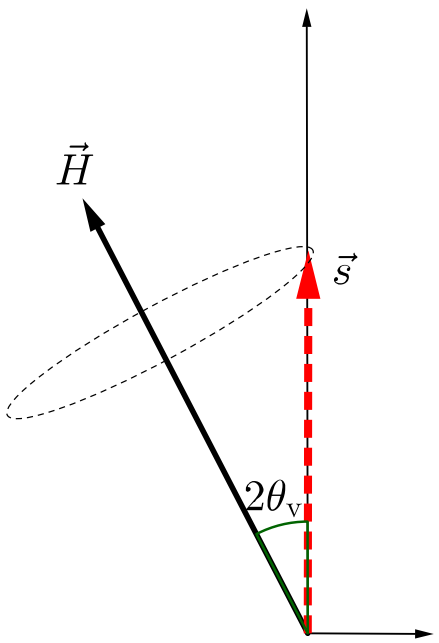

Figure 2.7: Vacuum oscillations in the flavor isospin picture. The flavor isospin of a neutrino starting with the electron flavor will precess around the static "Hamiltonian vector" $\vec{H}$, which gives a periodic flavor oscillation according to Eqn. 2.4.

Hamiltonian for the neutrino flavor evolution in the presence of dense matter is

$$\mathsf{H}^{(\rm f)} = \frac{\omega_{\rm v}}{2}\left(-\cos 2\theta_{\rm v}\sigma_3 + \sin 2\theta_{\rm v}\sigma_1\right) + \frac{\lambda(x)}{2}\sigma_3$$

$$\Rightarrow \vec{H} = \vec{H}_{\rm v} + \vec{H}_{\rm m}(x) = \omega_{\rm v}\begin{pmatrix} -\sin 2\theta_{\rm v} \\ 0 \\ \cos 2\theta_{\rm v} \end{pmatrix} + \begin{pmatrix} 0 \\ 0 \\ -\lambda(x) \end{pmatrix},$$

where $\vec{H}_{\rm v}$ is the vacuum contribution, and $\vec{H}_{\rm m}(x)$ is the matter potential contribution. The precession motion of the flavor isospin of the neutrino in the presence of dense matter is visualized in Fig. 2.8. The MSW resonance condition in Eqn. 2.18 corresponds to the senario that the overall "Hamiltonian vector" $\vec{H}$ is perpendicular to the third axis in flavor space. In this case, the flavor isospin rotates in the plane spanned by the second and third axes which gives maxium flavor oscillations

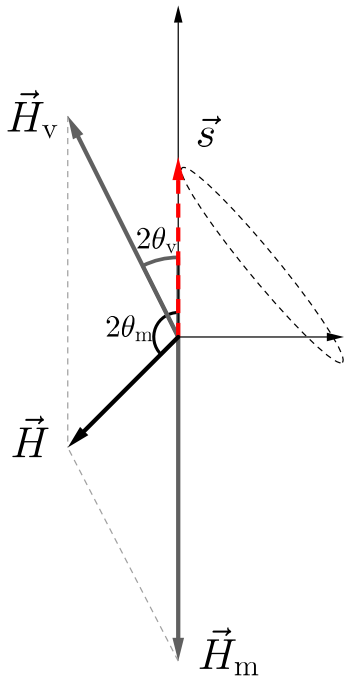

Figure 2.8: Neutrino oscillations in flavor isospin picture, with the presence of matter potential. The flavor isospin is denoted as red dashed arrow. It starts from electron flavor. The two gray vectors stand for the Hamiltonians of vacuum $\vec{H}_{\rm v}$ and matter $\vec{H}_{\rm m}$.

(see Fig. 2.9).

The adiabatic flavor evolution of the neutrino in varying matter density that was discussed in Sec. 2.3 can also be easily understood by the flavor-isospin picture. In the region where the matter density is high, the total "Hamiltonian vector" $\vec{H}$ points downward. Therefore, a neutrino produced in the electron flavor will experience very little oscillations because its flavor isospin $\vec{s}$ is almost anti-parallel to $\vec{H}$ (see Fig. 2.10a). If the matter density along the propagation trajectory of the neutrino decreases slowly, the $\vec{s}$ will stay anti-parallel to $\vec{H}$ as $\vec{H}$ rotates (see Fig. 2.10b). When the neutrino reaches the region with very low matter density, its flavor isospin becomes anti-parallel to $\vec{H}_{\rm v}$, which implies that the neutrino is in $|\nu_2\rangle$ (see Fig. 2.10).

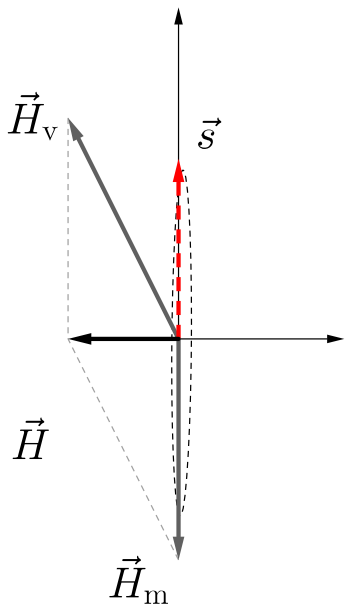

Figure 2.9: MSW resonance happens when electron neutrinos go through a critical matter density.

2.5 Summary

Neutrino oscillations in vacuum and in matter with a smooth profile have been explained. The neutrino oscillations phenomena reveals a secret of the nature of the neutrino, i.e., its flavor states are not the same as the propagation eigenstates of the Hamiltonian. As a result, a neutrino produced in the pure flavor state through weak interaction will not remain in the same flavor state as it propagates, but oscillate between different flavors. The problem of neutrino oscillations in an environment with rapidly varying matter densities is significant more difficult than that in a smooth profile. This will be discussed in the next chapter.

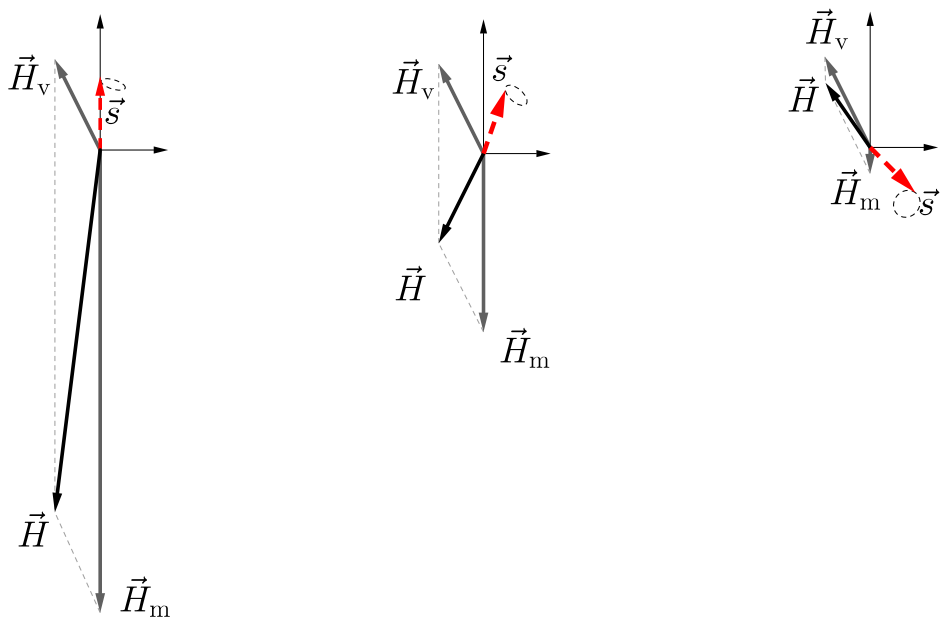

(a) High matter density (b) Medium matter density (c) Low matter density

Figure 2.10: Flavor isospin picture of neutrino oscillations in matter. $\vec{H}_{\rm v}$ is the vacuum contribution to Hamiltonian, and $\vec{H}_{\rm m}$ corresponds to the matter potential.

Chapter 3

Neutrino Oscillations with Oscillatory Matter Profiles

In certain regions inside a star or a supernova where convection is prominent, the matter density varies rapidly as a function of distance [31, 30]. The neutrino flavor evolution in such environments is qualitatively different than that with a smooth density profile [7, 9, 11, 18, 22, 25, 29]. For example, the flavor conversion of the neutrino is greatly enhanced if the matter density fluctuates with certain wave numbers. This is known as the parametric resonance [cite smirnov].

To understand this interesting phenomena I will first introduce the background matter basis where the equation of motion simplifies. After demonstrating the simplest example of the parametric resonance in the presence of a sinusoidal matter profile with the Rabi formula, I will explain the interference effect when there exist multiple Fourier modes in the matter profile. Then I will show how to use the Jacobi-Anger expansion to decompose an arbitrary matter profile into an infinite sum of Rabi modes and how to apply the Rabi formula in these scenarios.

3.1 Background Matter Basis

For a uniform matter density $\lambda(r) = \lambda_0$, one can define a matter basis in which the Hamiltonian is diagonalized:

$$\mathsf{H}^{(\mathrm{m})} = \mathsf{U}^\dagger \mathsf{H}^{(\mathrm{f})} \mathsf{U} = -\frac{\omega_\mathrm{m}}{2}\sigma_3, \tag{3.1}$$

where

$$\mathsf{U} = \begin{pmatrix} \cos\theta_\mathrm{m} & \sin\theta_\mathrm{m} \\ \sin\theta_\mathrm{m} & \cos\theta_\mathrm{m} \end{pmatrix} \tag{3.2}$$

with

$$\theta_\mathrm{m} = \frac{1}{2}\arctan\left(\frac{\sin 2\theta_\mathrm{v}}{\cos 2\theta_\mathrm{v} - \lambda_0/\omega_\mathrm{v}}\right),$$

and

$$\omega_\mathrm{m} = \omega_\mathrm{v}\sqrt{(\lambda_0/\omega_\mathrm{v} - \cos(2\theta_\mathrm{v}))^2 + \sin^2(2\theta_\mathrm{v})} \tag{3.3}$$

is the neutrino oscillation frequency in matter.

In the rest of the chapter, I will consider profiles of the form

$$\lambda(r) = \lambda_0 + \delta\lambda(r), \tag{3.4}$$

where $\delta\lambda(r)$ describes the fluctuation of the matter density. I will use the background matter basis defined in Eqn. 3.1 and Eqn. 3.3. In this basis, the Hamiltonian reads

$$\mathsf{H}^{(\mathrm{m})} = -\frac{\omega_\mathrm{m}}{2}\sigma_3 + \frac{1}{2}\delta\lambda(r)\cos 2\theta_\mathrm{m}\sigma_3 - \frac{1}{2}\delta\lambda(r)\sin 2\theta_\mathrm{m}\sigma_1. \tag{3.5}$$

In this chapter, I will focus on the transition probability between the background matter eigenstates

$$\begin{pmatrix} |\nu_\mathrm{L}\rangle \\ |\nu_\mathrm{H}\rangle \end{pmatrix} = \mathsf{U}^\dagger \begin{pmatrix} |\nu_\mathrm{e}\rangle \\ |\nu_\mathrm{x}\rangle \end{pmatrix}. \tag{3.6}$$

Given this transition probability, it is trivial to calculate the flavor conversion.

All the numerical examples in this chapter are calculated with $\sin^2(2\theta_\mathrm{v}) = 0.093$ and $\omega_\mathrm{v} = 3.75 \times 10^{-17}\mathrm{MeV}^2$.

3.2 Single Frequency Matter Profile and Rabi oscillations

In this section I will present a simple picture to explain neutrino parametric resonance in matter by utilizing the theory of Rabi oscillations. Rabi oscillations have been well studied in quantum optics [19]. It describes the transition between different quantum states due to an oscillatory external driving field, where maximum transition or resonance happens when the frequency of the external driving field equals the energy gap between two quantum states. In this section, I will first derive the Rabi oscillation transition probabilities using the neutrino flavor isospin method introduced in Ref. [16]. Then I will apply the results of Rabi oscillations to the neutrino oscillation with a single frequency matter profile.

3.2.1 Rabi Oscillations

Figure 3.1: A two-level quantum system that experiences the Rabi oscillation. The resonance happens when the frequency of the driving field ω equals the energy gap $\omega_R = \epsilon_2 - \epsilon_1$.

A two-level quantum system with energy gap $\delta\varepsilon = \omega_R$ can experience Rabi oscillations when light of frequency ω shines on it (see Fig. 3.1). The Hamiltonian for the system is

$$\mathsf{H}_R = -\frac{\omega_R}{2}\sigma_3 - \frac{A_R}{2}\left(\cos(k_R t + \phi_R)\sigma_1 - \sin(k_R t + \phi_R)\sigma_2\right), \tag{3.7}$$

where A_{R} and k_{R} are the amplitude and frequency of the driving field, respectively. The Hamiltonian H_{R} can be mapped into a vector using the flavor isospin picture:

$$\vec{H}_{\mathrm{R}} = \vec{H}_3 + \vec{H}_+,$$

where

$$\vec{H}_3 = \begin{pmatrix} 0 \\ 0 \\ \omega_{\mathrm{R}} \end{pmatrix} \quad \text{and} \quad \vec{H}_+ = \begin{pmatrix} A_{\mathrm{R}} \cos(k_{\mathrm{R}} t + \phi_{\mathrm{R}}) \\ -A_{\mathrm{R}} \sin(k_{\mathrm{R}} t + \phi_{\mathrm{R}}) \\ 0 \end{pmatrix}. \tag{3.8}$$

The vector $\vec{H}_3$ is the vector aligned with the third axis and $\vec{H}_+$ is a vector rotating in a plane perpendicular to $\vec{H}_3$ (see Fig. 3.2a). The wave function $\Psi = (\psi_1, \psi_2)^{\mathrm{T}}$ is also used to define the state vector $\vec{s}$

$$\vec{s} = \Psi^\dagger \frac{\vec{\sigma}}{2} \Psi \tag{3.9}$$

$$= \frac{1}{2} \begin{pmatrix} 2\,\mathrm{Re}\,(\psi_1^* \psi_2) \\ 2\,\mathrm{Im}\,(\psi_1^* \psi_2) \\ |\psi_1|^2 - |\psi_2|^2 \end{pmatrix} \tag{3.10}$$

The third component of $\vec{s}$, which is denoted as s_3, is within range $[-1/2, 1/2]$. The two limits, $s_3 = -1/2$ and $s_3 = 1/2$ stand for the two-level system in the high energy state and the low energy state, respectively. If the two-level system has equal probabilities to be in the high energy state and the low energy state, one has $s_3 = 0$. The equation of motion is a precession equation similar to Eqn. 2.24. In this example, the total "Hamiltonian vector" $\vec{H}_{\mathrm{R}}$ is not static since it has a rotating component $\vec{H}_+$. I need a better frame to understand the evolution of the state vector $\vec{s}$.

A more convenient frame is the one that corotates with $\vec{H}_+$, which is depicted in Fig. 3.2b. The equation of motion in this frame is

$$\frac{\mathrm{d}}{\mathrm{d}t}\vec{s} = \vec{s} \times (\vec{H}_3' + \vec{H}_+), \tag{3.11}$$

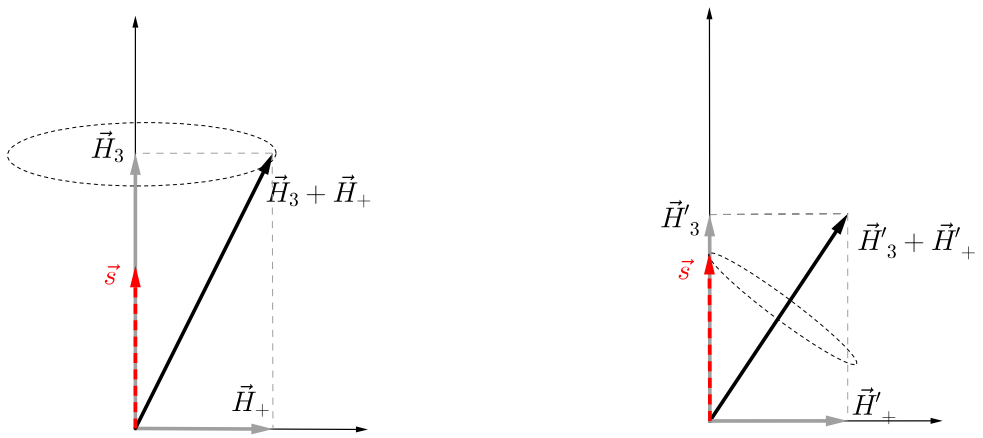

(a) Static frame (b) Corotatting frame

Figure 3.2: Rabi oscillations in different frames. The vectors $\vec{H}_3$ and $\vec{H}_+$ are defined in Eqn. 3.8. The red dashed vector $\vec{s}$ represents the quantum state of the system, and the black solid vectors are for the Hamiltonians in the corresponding frames.

where

$$\vec{H}'_3 = \begin{pmatrix} 0 \\ 0 \\ \omega_{\rm R} - k_{\rm R} \end{pmatrix}, \quad \text{and} \quad \vec{H}'_+ = \begin{pmatrix} A_{\rm R} \\ 0 \\ 0 \end{pmatrix}. \tag{3.12}$$

The state vector $\vec{s}$ precesses around the static vector $\vec{H}'_3 + \vec{H}'_+$ in this corotating frame with a frequency

$$\Omega_{\rm R} = \sqrt{|A_{\rm R}|^2 + (k_{\rm R} - \omega_{\rm R})^2}, \tag{3.13}$$

which is known as the Rabi frequency. Projecting the state vector $\vec{s}$ on to the third axis, I obtain

$$s_3 = \frac{1}{2} - \frac{|A_{\rm R}|^2}{\Omega_{\rm R}^2} \sin^2\left(\frac{\Omega_{\rm R}}{2} t\right). \tag{3.14}$$

Such a system has an analytical transition probability from the low energy state to the high energy state, known as the Rabi formula,

$$P(t) = \frac{1}{2}(1 - 2s_3(t)) = \frac{|A_{\rm R}|^2}{\Omega_{\rm R}^2} \sin^2\left(\frac{\Omega_{\rm R}}{2} t\right). \tag{3.15}$$

The amplitude A_{R} is the dominant factor of oscillation frequency when the system is close to resonance. The phase ϕ_{R} of the driving potential in Eqn. 3.7 has no effect on the transition probability since it only determines the initial phase of driving Hamiltonian vector $\vec{H}_{+}$. Fig. 3.3 shows two examples of Rabi oscillations.

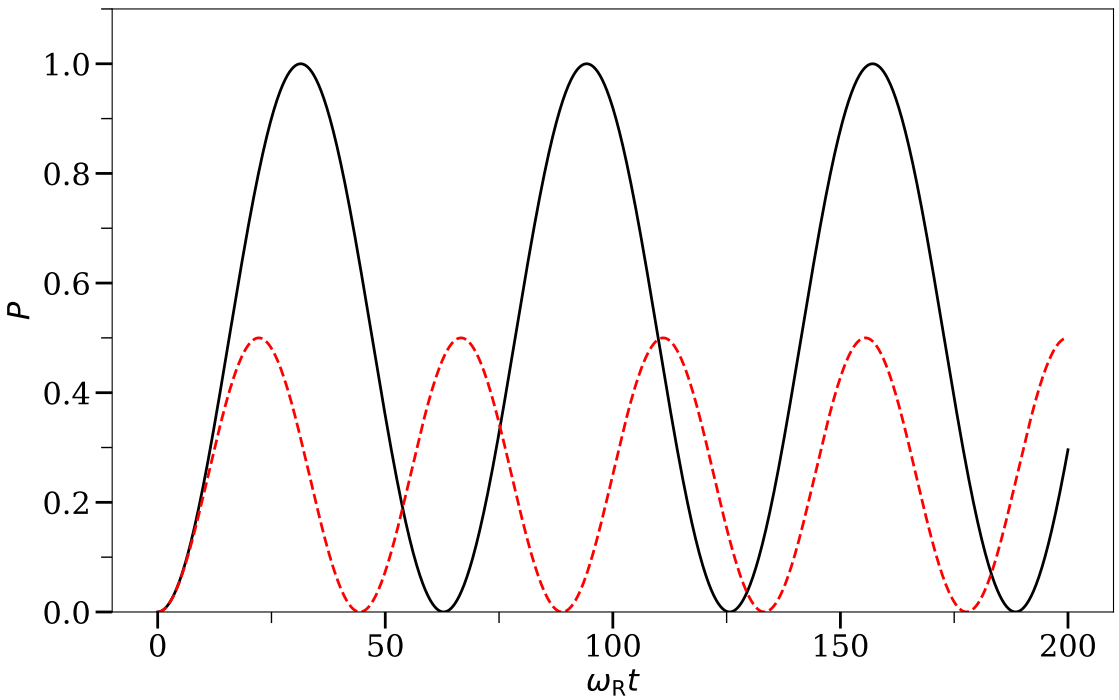

Figure 3.3: The transition probabilities P between the energy states of a two-level quantum system when external driving fields with frequencies $k_{\mathrm{R}} = \omega_{\mathrm{R}}$ and $k_{\mathrm{R}} = 1.1\omega_{\mathrm{R}}$ are applied, respectively. The amplitudes of the driving fields are $A_{\mathrm{R}} = 0.1\omega_{\mathrm{R}}$ in both cases.

Resonance of Rabi oscillations occurs when $\vec{H}_3' = 0$ in the corotating frame and $\vec{s}$ oscillates between $+1/2$ (the low energy state) and $-1/2$ (the high energy state). The amplitude of the driving field A_{R} determines the resonance width, as shown in Fig. 3.4. The transition amplitude is determined by relative detuning

$$D = \left| \frac{k_{\mathrm{R}} - \omega_{\mathrm{R}}}{A_{\mathrm{R}}} \right|. \tag{3.16}$$

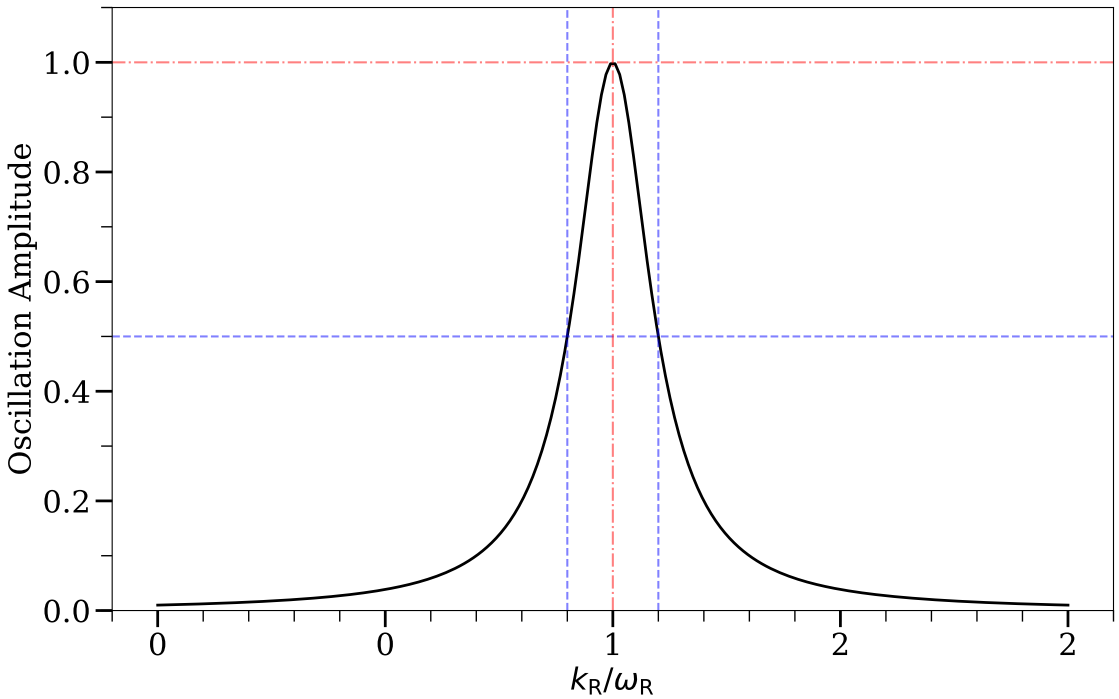

Figure 3.4: The amplitude of Rabi oscillations as a function of the frequency of the external driving field $k_{\rm R}$. The maximum amplitude occurs at $k_{\rm R}/\omega_{\rm R} = 1$. The resonance width is defined to be the difference of $k_{\rm R}$ at which the amplitudes are 1/2.

3.2.2 Interference Between the Driving Fields

In many cases, the two-level quantum system has more than one driving fields. Here I consider the Hamiltonian with two driving potentials:

$$\begin{aligned}\mathsf{H}_{\rm R} = &-\frac{\omega_{\rm R}}{2}\sigma_3 - \frac{A_1}{2}\left(\cos(k_1 t+\phi_1)\sigma_1 - \sin(k_1 t+\phi_1)\sigma_2\right)\\ &-\frac{A_2}{2}\left(\cos(k_2 t+\phi_2)\sigma_1 - \sin(k_2 t+\phi_2)\sigma_2\right).\end{aligned}$$

I decompose it into $\vec{H}_{\rm R} = \vec{H}_3 + \vec{H}_1 + \vec{H}_2$, where

$$\vec{H}_1 = \begin{pmatrix} A_1\cos(k_1 t+\phi_1)\\ -A_1\sin(k_1 t+\phi_1)\\ 0\end{pmatrix} \quad \text{and} \quad \vec{H}_2 = \begin{pmatrix} A_2\cos(k_2 t+\phi_2)\\ -A_2\sin(k_2 t+\phi_2)\\ 0\end{pmatrix}.$$

I will assume that the first potential $\vec{H}_1$ is almost on resonance, and the second potential $\vec{H}_2$ is off resonance, i.e.,

$$D_1 \lesssim 1 \quad \text{and} \quad D_2 \gg 1, \tag{3.17}$$

where

$$D_i \equiv \frac{|k_i - \omega_{\rm R}|}{|A_i|} \tag{3.18}$$

is the relative detuning of the ith driving field.

Although the second driving field is off resonance, it can interfere with the Rabi oscillation caused by the first driving field. To see this effect, I will use the frame that corotates with $\vec{H}_2$. In the corotating frame, the two driving fields have frequencies $k_1' = k_1 - k_2$ and $k_2' = 0$, respectively, and $\vec{H}_3' = (0, 0, \omega_{\rm R} - k_2)^{\rm T}$. Obviously, the Hamiltonian vector in this corotating frame is similar to Eqn. 3.2.1 except with the replacements

$$\vec{H}_3 \to \vec{H}_3' + \vec{H}_2' \quad \text{and} \quad \vec{H}_+ \to \vec{H}_1'. \tag{3.19}$$

I will further assume that $|A_2| \ll \omega_{\rm R}$ so that the new energy gap is

$$\begin{aligned} \tilde{\omega}_{\rm R}' &\equiv |\vec{H}_3' + \vec{H}_2'| \\ &= \text{sign}(\omega_{\rm R} - k_2)\sqrt{(\omega_{\rm R} - k_2)^2 + A_2^2} \\ &\approx \omega_{\rm R} - k_2 + \frac{1}{2}\frac{A_2^2}{\omega_{\rm R} - k_2}, \end{aligned} \tag{3.20}$$

where I kept only up to the first order of the Taylor series. I can calculate the new relative detuning of the system to be

$$\begin{aligned} D' &= \frac{|k_1' - \tilde{\omega}_{\rm R}'|}{|A_1|} \\ &\approx \left| \frac{k_1 - \omega_{\rm R}}{A_1} + \frac{A_2^2}{2A_1(k_2 - \omega_{\rm R})} \right|. \end{aligned} \tag{3.21}$$

One can adjust frequency of the off-resonance driving field k_2 to decrease or increase D so that the system is close to or further away from the resonance.

3.2.3 Single Frequency Matter Profile

I will examine the neutrino flavor conversions in a single frequency matter profile $\delta\lambda(r) = \lambda_1 \cos(k_1 r)$. The Hamiltonian in background matter basis becomes

$$\mathsf{H}^{(\mathrm{m})} = -\frac{\omega_\mathrm{m}}{2}\sigma_3 + \frac{1}{2}\lambda_1 \cos(k_1 r)\cos 2\theta_\mathrm{m}\sigma_3 - \frac{1}{2}\lambda_1 \cos(k_1 r)\sin 2\theta_\mathrm{m}\sigma_1. \tag{3.22}$$

As will be proved later, the varying σ_3 term $\frac{1}{2}\lambda_1 \cos(k_1 r)\cos 2\theta_\mathrm{m}\sigma_3$ in the above Hamiltonian, which is the varying energy gap due to varying matter density fluctuations, has little effect on the transition probabilities when the system is not too far from resonance[1]. With the varying σ_3 term removed, the single frequency matter perturbation neutrino flavor conversion system will be reduced to a Rabi oscillation system. The external driving field frequency is $\pm k_1$ and the energy gap is ω_m. I can decompose $\cos(k_1 r)$ into two exponential functions so that we have two external driving frequencies k_1 and $-k_1$. By neglecting the off-resonance frequency $-k_1$, the Hamiltonian can be simplified to

$$\begin{aligned}
\mathsf{H}^{(\mathrm{m})} &\to -\frac{\omega_\mathrm{m}}{2}\sigma_3 - \frac{1}{2}\lambda_1 \sin 2\theta_\mathrm{m}\cos(k_1 r)\sigma_1 \\
&\to -\frac{\omega_\mathrm{m}}{2}\sigma_3 - \frac{1}{2}A_1 \exp(\mathrm{i}k_1 r)\sigma_1 \\
&= -\frac{\omega_\mathrm{m}}{2}\sigma_3 - \frac{1}{2}A_1 \cos(k_1 r)\sigma_1 + \frac{1}{2}A_1 \sin(k_1 r)\sigma_2,
\end{aligned} \tag{3.23}$$

where I have used

$$A_1 = \frac{\lambda_1 \sin 2\theta_\mathrm{m}}{2}. \tag{3.24}$$

Now I have reduced the neutrino oscillations to Rabi oscillations. The resonance happens when the energy gap ω_m is close to the external driving field frequency k_1, i.e., $\omega_\mathrm{m} \sim k_1$. As long as the resonance condition is satisfied, the transition probability between the two mass states should be predicted well using Rabi formula. To show that this conjecture of simplifying neutrino flavor conversions to Rabi oscillations is correct, I calculated the transition probabilities of the neutrinos described

[1]For the purpose of this section, I will consider the case when k_1 is not far away from resonance.

by Eqn. 3.24 numerically, and compared them with Rabi formula Eqn. 3.15 from the Rabi oscillations described by Eqn. 3.7.

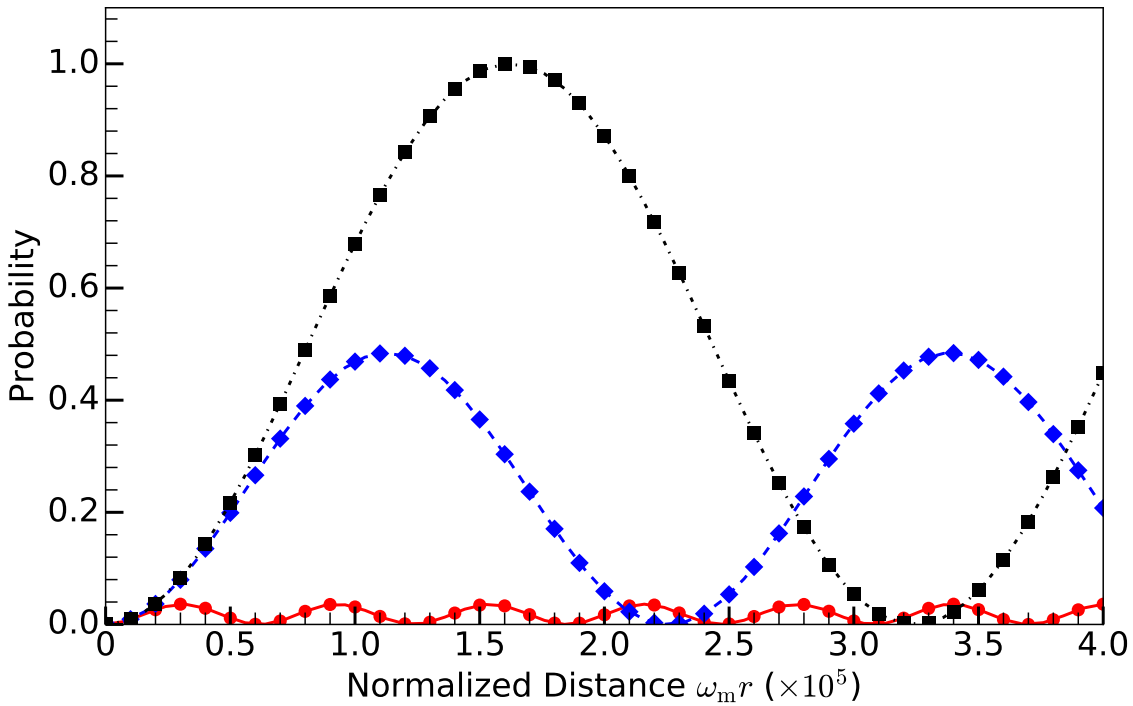

Figure 3.5: Single frequency matter profile and Rabi oscillation. The markers are numerical results for the transition probabilities between two background mass eigenstates for the neutrinos with matter perturbation $A_1 \sin(k_1 r)$. The dots, diamonds, and squares are for $k_1 = \omega_m$, $k_1 = (1 - 2 \times 10^{-5})\omega_m$, and $k_1 = (1 - 10^{-4})\omega_m$ respectively. The lines are the predictions using Rabi formula. During the calculation, λ_0 is set to 0.5 of the MSW resonance potential $\lambda_{MSW} = \omega_v \cos 2\theta_v$ and mixing angle is chosen so that $\sin^2(2\theta_v) = 0.093$.

In Fig. 3.5, I have plotted the numerical results using markers as well as the prediction using Rabi formula using lines. The agreement between numerical solutions of neutrino transitions between mass states and Rabi formula will be explained more precisely in Sec. 3.4. For now, we address the significance of relative detuning $D = |k_1 - \omega_m|/|A_1|$, which is rigoriously defined in Eqn. 3.16. $D \to 0$ indicates that the neutrino oscillation is very close to resonance, while $D \to \infty$ indicates that the neutrino oscillation is far away from resonance. The corresponding relative de-

tunings in Fig. 3.5 are 0, 1.0, and 5.2 for $k_1 = \omega_{\rm m}$, $k_1 = (1 - 2 \times 10^{-5})\omega_{\rm m}$, and $k_1 = (1 - 10^{-4})\omega_{\rm m}$.

For a single-frequency perturbation in the matter profile $\lambda(r) = \lambda_1 + \lambda_1 \sin(k_1 r)$, P. Krastev and A. Smirnov concluded that the parametric resonance condition is $\omega_{\rm m} \sim n k_1$, if instantaneous $\omega_{\rm m,inst}(r)$ associated with the matter profile at distance r varies slowly [7]. This condition is exactly the Rabi resonance condition when $n = 1$, as such condition matches the driving field frequency to the energy split. Higher order effects are explained in Sec. **??**.

3.3 Multi-frequency Matter Profiles

The approach applied to single frequency matter profile also helps with the understanding of multi-frequency matter profile. However, multi-frequency matter profile leads to multiple modes of Rabi oscillations, even with our simplified approach by dropping the varying σ_3 term in Hamiltonian. In this section, we examine the neutrino oscillations in multi-frequency matter profiles using the interference effects discussed in Sec. 3.2.1.

The Hamiltonian for neutrino oscillations in matter background with two frequencies is

$$\begin{aligned} \mathsf{H}^{(\rm m)} = &- \frac{\omega_{\rm m}}{2}\sigma_3 + \frac{1}{2}\left(\lambda_1 \cos(k_1 r) + \lambda_2 \cos(k_2 r)\right) \cos 2\theta_{\rm m} \sigma_3 \\ &- \frac{1}{2}\left(\lambda_1 \cos(k_1 r) + \lambda_2 \cos(k_2 r)\right) \sin 2\theta_{\rm m} \sigma_1. \end{aligned} \tag{3.25}$$

I will drop the varying σ_3 terms for the same reason as in single frequency matter profile case. The Hamiltonian becomes the two-frequency Rabi oscillation Hamiltonian,

$$\mathsf{H}^{(\rm m)} = -\frac{\omega_{\rm m}}{2}\sigma_3 - \frac{1}{2}\left(\lambda_1 \cos(k_1 r) + \lambda_2 \cos(k_2 r)\right) \sin 2\theta_{\rm m} \sigma_1. \tag{3.26}$$

The oscillation probabilities can be predicted by the Rabi formula Eqn. 3.15 with the new relative detuning calculated with Eqn. 3.22. It can be verified by comparing the numerical solution and estimation using Rabi formula. However, I am most interested in the amplitude change due to $\mathbf{H}_2$ mode. Relative detuning is the only variable that I need to calculate the amplitude, hence I only compare the numerical results with estimated amplitudes using $1/(1+D'^2)$. To verify the condition, I choose the first rotating perturbation to satisfy the resonance condition $k_1 = \omega_{\rm m}$, the condition for the second rotating field shifting the system out of resonance is that the relative detuning becomes larger than 1, which leads to

$$|A_2| \geq \sqrt{2\omega_{\rm m}|A_1(k_2-\omega_{\rm m})|} \equiv A_{2,\rm Critical}. \tag{3.27}$$

I expect the transition amplitude to decrease as we have larger $|A_2|$.

I choose the two modes where the first one has amplitude $A_1 = 10^{-4}\omega_{\rm m}$ and frequency $k_1 = \omega_{\rm m}$. With a small amplitude of the second frequency, $A_2 = 10^{-4}\omega_{\rm m}$, and large frequency $k_2 = 10\omega_{\rm m}$, I obtain almost full resonance. As shown in Eqn. 3.22, larger A_2 leads to more effective destruction effect. In Fig. 3.6, I am showing the full numerical solution of neutrino oscillations in two-frequency matter background, and the prediction of oscillations using Rabi formula, which is a good match to the numerical results. To show the importance of relative detuning, I also calculated the relative detuning for each cases, which are 0.06, 0.6, 1.4 for the lines from top to down. Notice that the width of each cases doesn't change since I kept A_1 fixed for each calculation, which indicates that the decreasing in transition amplitude is because of the increasing in detuning.

Adding a second frequency to the matter density profile can also be constructive. I calculated an example with two frequencies in matter density profile, so that the Hamiltonian is

$$\mathsf{H}^{(\rm m)} = -\frac{\omega_{\rm m}}{2}\sigma_3 - \left(\frac{A_1}{2}\cos(k_1 r) + \frac{A_2}{2}\cos(k_2 r)\right)\sigma_1 + \left(\frac{A_1}{2}\sin(k_1 r) + \frac{A_2}{2}\sin(k_2 r)\right)\sigma_2.$$

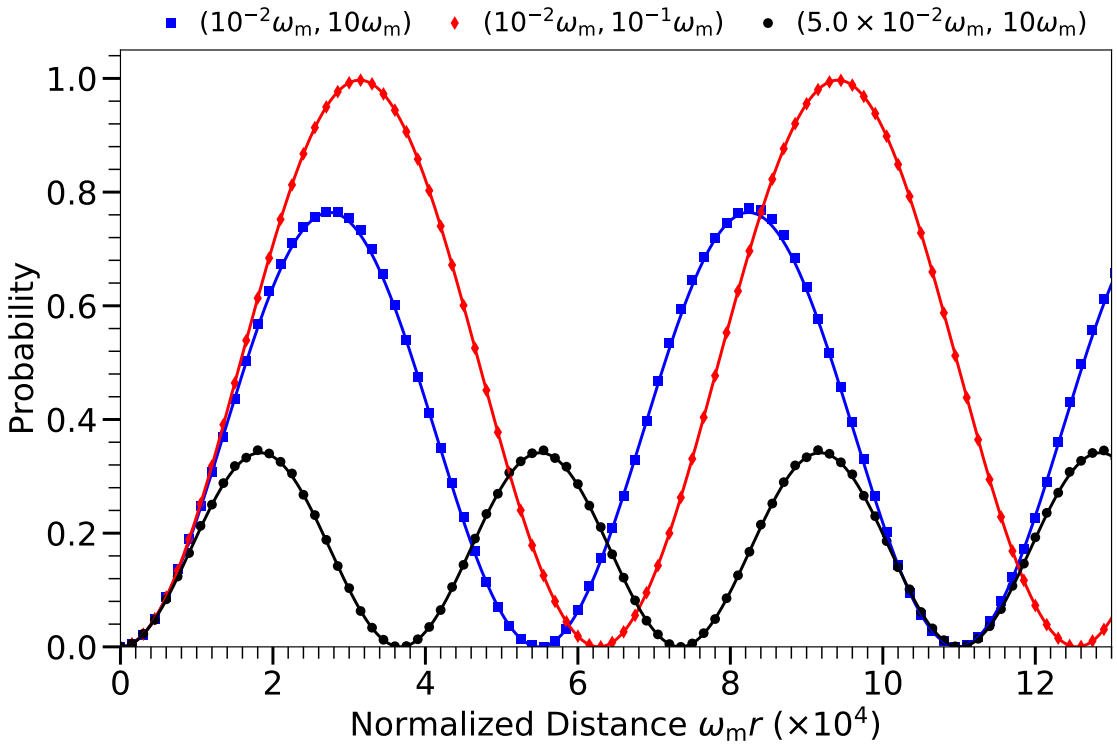

Figure 3.6: Reduction of transition amplitudes due to interference. Blue squares, red diamonds, and black dots are for $A_2 = 10^{-2}\omega_m$, $k_2 = 10\omega_m$, $A_2 = 10^{-2}\omega_m$, $k_2 = 10^{-1}\omega_m$, $A_2 = 5.0\times, and 10^{-2}\omega_m$, $k_2 = 10\omega_m$, respectively. The lines are the corresponding Rabi formula predictions. In all the calculations, I used $A_1 = 10^{-4}\omega_m$, $k_1 = \omega_m$. During the calculations, Λ_0 is set to half of the MSW resonance potential, $\Lambda_0 = \frac{1}{2}\lambda_{MSW} = \frac{1}{2}\omega_v \cos 2\theta_v$.

I choose two matter profile frequencies that are off resonance and producing large relative detuning,

$$A_1 = 0.025, \qquad k_1 = 0.95, \qquad A_1 = 0.4, \qquad k_2 = 2.6. \tag{3.28}$$

The oscillation amplitude for each mode being much smaller than 1. However, the combined two frequencies case produces oscillations are resonance (c.f. Fig. 3.7), since the relative detuning for the combined two frequencies case is 0.

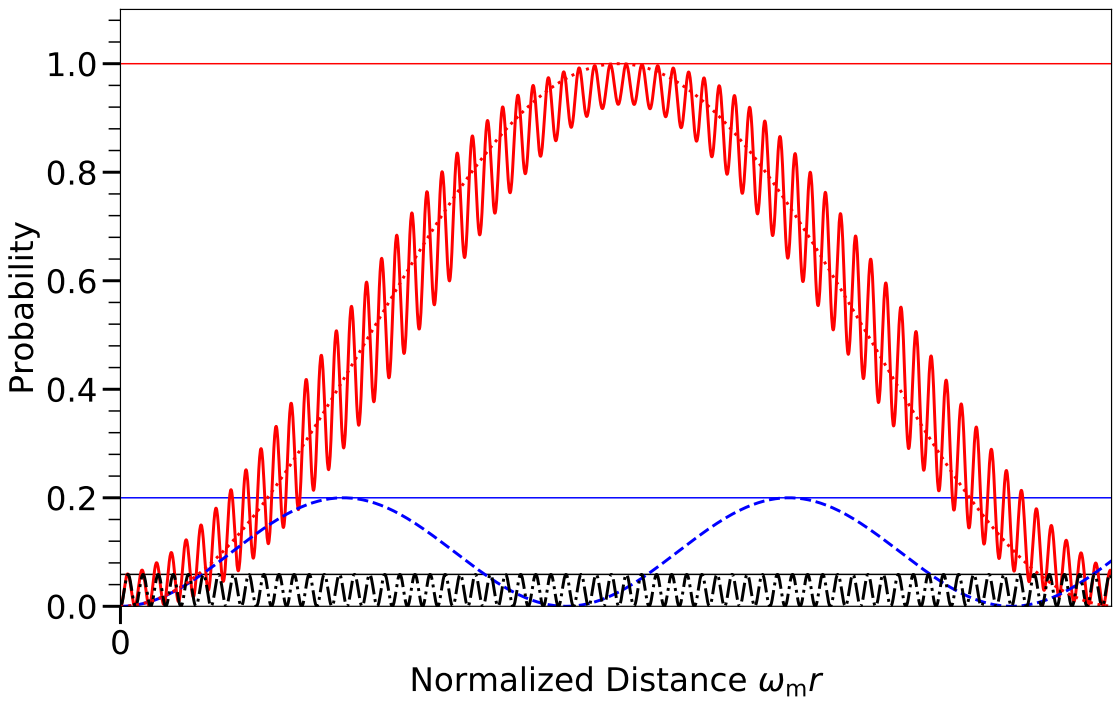

Figure 3.7: Constructive interference for two frequencies in matter density profile. The solid red line, dashed blue line, dash-dotted black line, are the transition probability for two frequencies combined, the first frequency k_1 only, the second frequency k_2 only. The amplitudes of each frequency are $A_1 = 0.4$, $A_2 = 2.6$ respectively. The grid lines are the oscillations amplitudes predicted by Rabi formula. The dotted red line is the oscillations predicted by Rabi formula for the two combined frequencies.

3.4 Rabi Basis and Jacobi-Anger expansion

With the intuition of the Rabi oscillations itself as well as the interference between different modes of Rabi oscillations shown in Sec. 3.3, I can interpret the transition probabilities of any matter profile more precisely if the system can be exactly decomposed into multiple Rabi oscillations. Kneller et al. provided a method to achieve this goal [25], namely the Jacobi-Anger expansion. While they used the Jacobi-Anger expansion to calculate the neutrino oscillations in single frequency matter profiles through complicated calculation, I use a different approach that motivates

us to use the Jacobi-Anger expansion and simplifies the concepts and calculations. In this section, I will first show that a better basis can be found for the interpretation of neutrino oscillations in matter. Then, I will show that the neutrino oscillations in matter can be decomposed into superpositions of Rabi oscillations by applying the Jacobi-Anger expansion.

3.4.1 Rabi Basis

For neutrino oscillations with a general matter potential (see Eqn. 3.5), we apply an unitary transformation

$$\mathsf{U} = \begin{pmatrix} e^{-\mathrm{i}\eta(r)} & 0 \\ 0 & e^{\mathrm{i}\eta(r)} \end{pmatrix}. \tag{3.29}$$

I can also define a new basis $\left(|\nu_{\mathrm{r1}}\rangle\,, |\nu_{\mathrm{r2}}\rangle\right)^{\mathrm{T}}$, which is related to the background matter basis through U:

$$\begin{pmatrix} |\nu_{\mathrm{r1}}\rangle \\ |\nu_{\mathrm{r2}}\rangle \end{pmatrix} = \mathsf{U}^{\dagger} \begin{pmatrix} |\nu_{\mathrm{L}}\rangle \\ |\nu_{\mathrm{H}}\rangle \end{pmatrix}. \tag{3.30}$$

For convenience, I name this unitary transformation in Eqn. (3.30) Rabi transformation as well as the new basis in Eqn. (3.31) the Rabi basis. This transformation is a rotation with generator $\exp\left(-\mathrm{i}\frac{\sigma_3}{2}\cdot 2\eta\right)$, thus it doesn't change σ_3 terms themselves. Due to its dependence on r, the left side of the Schrödinger equation obtains an extra term other than the derivative, which can be used to cancel the varying σ_3 term, i.e., $\delta\lambda(r)\cos 2\theta_{\mathrm{m}}\sigma_3/2$. In the flavor isospin picture, the transform brings the neutrino states into a rotating frame so that the varying energy gap due to the fluctuating matter density is exactly cancelled by rotation of the frame. By remove the varying σ_3 term in this way, the energy gap in the Rabi basis becomes a constant energy gap. Another advantage of this transformation is that the transition probability from light state to heavy state in background matter basis is easily calculated as $P_{\mathrm{L}\to\mathrm{H}}(x) = |e^{i\eta}\psi_{\mathrm{r2}}(x)|^2 = |\psi_{\mathrm{r2}}(x)|^2$. One can easily show that the transition

probability between two eigenstates in the Rabi basis is the same as the transition probability between two eigenstates in background matter basis, given the initial condition that the system is in low energy state.

In the Rabi basis, the Schrödinger equation is

$$\begin{aligned}&\begin{pmatrix}\frac{\mathrm{d}\eta}{\mathrm{d}r} & 0\\ 0 & -\frac{\mathrm{d}\eta}{\mathrm{d}r}\end{pmatrix}\begin{pmatrix}\psi_{\mathrm{R1}}\\ \psi_{\mathrm{R2}}\end{pmatrix}+\mathrm{i}\frac{\mathrm{d}}{\mathrm{d}r}\begin{pmatrix}\psi_{\mathrm{R1}}\\ \psi_{\mathrm{R2}}\end{pmatrix}\\ =&\left[-\frac{\omega_{\mathrm{m}}}{2}\sigma_3+\frac{\delta\lambda}{2}\cos 2\theta_{\mathrm{m}}\sigma_3-\frac{\delta\lambda}{2}\sin 2\theta_{\mathrm{m}}\begin{pmatrix}0 & e^{2\mathrm{i}\eta}\\ e^{-2\mathrm{i}\eta} & 0\end{pmatrix}\right]\begin{pmatrix}\psi_{\mathrm{R1}}\\ \psi_{\mathrm{R2}}\end{pmatrix},\end{aligned}$$

in which the varying diagonal elements in Hamiltonian can be eliminated by choosing $\eta(r)$ properly, i.e.,

$$\eta(r)-\eta(0)=\frac{\cos 2\theta_{\mathrm{m}}}{2}\int_0^r\delta\lambda(\tau)\mathrm{d}\tau, \tag{3.31}$$

which is used to simplify the Schrödinger equation:

$$\mathrm{i}\frac{\mathrm{d}}{\mathrm{d}r}\begin{pmatrix}\psi_{\mathrm{r1}}\\ \psi_{\mathrm{r2}}\end{pmatrix}=\left[-\frac{\omega_{\mathrm{m}}}{2}\sigma_3-\frac{\delta\lambda}{2}\sin 2\theta_{\mathrm{m}}\begin{pmatrix}0 & e^{2\mathrm{i}\eta}\\ e^{-2\mathrm{i}\eta} & 0\end{pmatrix}\right]\begin{pmatrix}\psi_{\mathrm{r1}}\\ \psi_{\mathrm{r2}}\end{pmatrix}. \tag{3.32}$$

3.4.2 Single Frequency Matter Profile and Jacobi-Anger Expansion

For a rigorous analysis of neutrino oscillations in oscillatory matter profiles, I will need the Jacobi-Anger expansion. Jacobi-Anger expansion is used to expand exponential functions of the form $e^{\mathrm{i}r\cos(\phi)}$ using the basis $e^{\mathrm{i}n\phi}$,

$$e^{\mathrm{i}r\cos(\phi)}=\sum_{n=-\infty}^{\infty}\mathrm{i}^n J_n(r)e^{\mathrm{i}n\phi}. \tag{3.33}$$

J. Kneller and K. Patton et al. used this method to calculate the transition probabilities of neutrinos in oscillatory matter profile [22, 25, 29]. In this subsection, I

will review the method of Jacobi-Anger expansion and its application to neutrino oscillations, using a different formalism.

For the purpose of this section, I will demonstrate the decomposition of single frequency matter profile with potential $\delta\lambda(r) = \lambda_1 \sin(k_1 r)$. The equation of motion has been derived and presented in Eqn. 3.33. For single frequency matter profile, the Hamiltonian is

$$\mathsf{H}^{(\mathrm{R})} = \frac{\omega_\mathrm{m}}{2}\sigma_3 - \frac{\sin 2\theta_\mathrm{m}\lambda_1 \sin(k_1 r)}{2}\begin{pmatrix} 0 & e^{2\mathrm{i}\eta(r)} \\ e^{-2\mathrm{i}\eta(r)} & 0 \end{pmatrix}, \tag{3.34}$$

where $\eta(r) = -\lambda_1 \cos 2\theta_\mathrm{m} \cos(k_1 r)/(2k)$. The $\exp(\mathrm{i}z\cos(k_1 r))$-like term in the Hamiltonian can be decomposed into linear combinations of terms that are proportional to $\exp(\mathrm{i}nk_1 r)$. The term $e^{2\mathrm{i}\eta(r)}$ is

$$\exp\left(\mathrm{i}\frac{\lambda_1 \cos 2\theta_\mathrm{m}}{k_1}\cos(k_1 r)\right) = \sum_{n=-\infty}^{\infty} (-\mathrm{i})^n J_n\left(\frac{\lambda_1 \cos 2\theta_\mathrm{m}}{k_1}\right) e^{\mathrm{i}nk_1 r}, \tag{3.35}$$

where I have used the relation

$$J_n(-x) = (-1)^n J_n(x). \tag{3.36}$$

With the expansion, the Hamiltonian becomes a Rabi oscillation with infinite driving frequencies,

$$\mathsf{H}^{(\mathrm{R})} = -\frac{\omega_\mathrm{m}}{2}\sigma_3 - \frac{1}{2}\sum_{n=-\infty}^{\infty} B_n \begin{pmatrix} 0 & \Phi_n e^{\mathrm{i}nk_1 r} \\ \Phi_n^* e^{-\mathrm{i}nk_1 r} & 0 \end{pmatrix}, \tag{3.37}$$

where

$$B_n = \tan 2\theta_\mathrm{m} n k_1 J_n\left(\frac{\lambda_1}{k_1}\cos 2\theta_\mathrm{m}\right), \tag{3.38}$$

$$\Phi_n = e^{i\pi(3n/2+1)}, \tag{3.39}$$

I have used

$$J_{n-1}(x) + J_{n+1}(x) = \frac{2n}{x} J_n(x) \tag{3.40}$$

in the derivation. The coefficient Φ_n doesn't play any role for the reason discussed in Sec. 3.2.1. Any phases in the matter potential would also go into Φ_n, hence phases of matter profile can be neglected. In the Hamiltonian, the first term describes the energy gap, while the second term is the summation of many driving fields. For each of the driving fields, the resonance width is $|B_n|$. In fact, it is straightforward to prove that the width drops very fast as a function of n since the Bessel function can be approximated as

$$J_n(n\text{sech}\,\alpha) \sim \frac{e^{n(\tanh\alpha-\alpha)}}{\sqrt{2\pi n\tanh\alpha}} \tag{3.41}$$

for large n [20]. Thus the higher order modes are usually insignificant.

When the matter potential provides one dominate resonance mode and without significant interference between the resonance mode and the other modes, all off-resonance modes can be dropped without significantly changing the transition probabilities. However, as we have shown previously in Sec. 3.2.1, interference might happen between different modes and interferences were measured with a criteria. In the following subsections, I will discuss the work I have done based on this expansion. First of all, I will explain the approximations used in Eqn. **??** to simplify the Hamiltonian. Then I will explore the interferences between modes.

3.4.3 Single Frequency Matter Profile Revisited

Even for the single frequency matter profile, there are two modes of Rabi oscillations $\pm k_1$, under the approximation that the varying σ_3 term in Hamiltonian is neglected, as mentioned in Sec. 3.2.1. The three examples calculated in Fig. 3.5 are almost exact since the modification of relative detuning for the k_1 mode that we kept, due to the far off resonance mode $-k_1$ that I neglected, is tiny. Since I have derived the interference effect in Sec. 3.2.1, the approximations can be justified quantitatively using Eqn. 3.22.

In order for a mode to have a significant effect on the transition probabilities, we require it to has large relative detuning D, and a large oscillation wavelength compared to the size of the physical system. Relative detuning for each mode is calculated as

$$D_n = \frac{|nk_1 - \omega_{\rm m}|}{B_n} \tag{3.42}$$

for single frequency matter profile. For modes with small relative detuning, they are important since they might lead to full transition. However, the full transition requires at least a distance of the order of the wavelength of the oscillation. Suppose we have a mode that has zero relative detuning, but with a oscillation wavelength much larger than the size of the neutrino oscillations system, such a mode would never have the chance to accumulate a large transition probability within the region of interest. By utilizing the theory of Rabi oscillation, we know that the oscillation wavelength of each mode is determined by the Rabi frequency

$$\Omega_{\{n_a\}} = |B_{\{n_a\}}|\sqrt{1 + D^2_{\{n_a\}}}. \tag{3.43}$$

Thus modes that has much larger oscillation wavelength are not subjected to be considered even though their relative detunings are close to zero. While we can always approximate the oscillations by including more modes with large relative detuning and neglecting the modes with wavelength much longer than the size of physical system, such effort is not always necessary.

In Table. 3.1 I calculated the relative detunings of the three cases in Fig. 3.5, where $n = \pm 1$ are for the $\pm k_1$ modes in the Hamiltonian Eqn. 3.24. The D'_1 is the shifted relative detuning of the first mode with $n = 1$ due to other mode. It clearly shows that the first mode takes the whole system so that the approximation of neglecting the varying σ_3 terms in Hamiltonian is accurate enough. One can also show that the interference effect due to higher order modes is negligible, since they

$k_1 = \omega_{\rm m}$				$k_1 = (1 - 2 \times 10^{-5})\omega_{\rm m}$				$k_1 = (1 - 10^{-4})\omega_{\rm m}$			
n	D	D_1'	$2\pi\omega_{\rm m}/\Omega_n$	n	D	D_1'	$2\pi\omega_{\rm m}/\Omega_n$	n	D	D_1'	$2\pi\omega_{\rm m}/\Omega_n$
1	0	-	3.2×10^5	1	1	-	2.2×10^5	1	5.2	-	6.2×10^4
-1	10^5	4.8×10^{-6}	3.1	-1	10^5	1	3.1	-1	10^5	5.2	3.1
2	1.1×10^9	2.1×10^{-14}	6.3	2	1.1×10^9	1	6.3	2	1.1×10^9	5.2	6.3
-2	3.4×10^9	6.9×10^{-15}	2.1	-2	3.4×10^9	1	2.1	-2	3.4×10^9	5.2	2.1

Table 3.1: Relative detuning and oscillation wavelength of each mode for single frequency matter profile.

do not change the relative detuning of the most significant modes. It confirms the results I observed in Fig. 3.5 that the change of the relative detuning due to the $-k_1$ mode is not observable.

In Sec. 3.2, I discussed the single frequency matter potential $\lambda = \lambda_0 + \lambda_1 \sin(k_1 r)$ by removing the varying σ_3 term by arguing that this term has no effect on transition probabilities when the system is close to resonance, $k_1 \sim \omega_{\rm m}$. The reason is that only the first mode $n = 1$ is on resonance when $k_1 = \omega_{\rm m}$ and all other modes are far from resonance, thus

$$\begin{aligned} \mathsf{H}^{\rm R} &\approx -\frac{\omega_{\rm m}}{2}\sigma_3 - \frac{1}{2}B_1 \begin{pmatrix} 0 & \Phi_1 e^{ik_1 r} \\ \Phi_1^* e^{-ik_1 r} & 0 \end{pmatrix} \\ &\approx -\frac{\omega_{\rm m}}{2}\sigma_3 - \frac{A_1}{2}\cos(k_1 r)\sigma_1 + \frac{A_1}{2}\sin(k_1 r)\sigma_2, \end{aligned} \tag{3.44}$$

where A_1 is defined in Eqn. (3.25) and approximation

$$J_1\left(\frac{\lambda_1}{k_1}\cos(2\theta_{\rm m})\right) \approx \frac{\lambda_1}{2k_1}\cos(2\theta_{\rm m})$$

for $\lambda_1 \cos(2\theta_{\rm m})/k_1 \ll 1$ is used in the last step. Thus we reach a similar equation to the approximation we used in Sec. 3.2. $\lambda_1 \cos(2\theta_{\rm m})/k_1 \ll 1$ corresponds to small resonance width for Eqn. (3.24) and also Eqn. (3.45) so that the interferences are small by Eqn. 3.22.

3.4.4 Multi-frequency Matter Profile Revisited

For multi-frequency matter profiles $\delta\lambda(r) = \sum_n \lambda_n \sin(k_n r)$, the derivation is the same as the derivation for single frequency matter profiles but with more tedious math. The Hamiltonian in Rabi basis is

$$\mathsf{H}^{(\mathrm{R})} = -\frac{\omega_{\mathrm{m}}}{2}\sigma_3 + \begin{pmatrix} 0 & h \\ h^* & 0 \end{pmatrix}, \tag{3.45}$$

where the off diagonal element h is

$$h = \frac{\sin 2\theta_{\mathrm{m}}}{2} \sum_a \lambda_a \sin(k_a x) \prod_a \sum_{n=-\infty}^{\infty} (-i)^n J_n(z_{k_a}) e^{in(k_a x)} \tag{3.46}$$

Using the relations of Bessel functions in Eqn. 3.41, I can decompose h into two terms

$$h = -\sum_{n_1=-\infty}^{\infty} \sum_{n_2=-\infty}^{\infty} (-\mathrm{i})^{\sum_a n_a} \frac{\tan 2\theta_{\mathrm{m}}}{2} \sum_a n_a k_a \tag{3.47}$$

$$J_{n_1}(\lambda_1 \cos 2\theta_{\mathrm{m}}/k_1) J_{n_2}(\lambda_2 \cos 2\theta_{\mathrm{m}}/k_2) e^{\mathrm{i}\sum_a n_a k_a r}. \tag{3.48}$$

The arguments that I applied to single frequency matter profile are still valid for multi-frequency matter profiles. For completeness of this section, I will present one example of multi-frequency matter profile. One of the multi-frequency matter profiles that has been well studied is the castle wall matter profile. I can decompose the periodic castle wall matter profile into many Fourier modes and study the interference effect. The potential shown in Fig. 3.8 is defined as,

$$\lambda(r) = \begin{cases} \Lambda_1, & -\frac{X_1}{2} + nX \le r \le \frac{X_1}{2} + nX \\ \Lambda_2, & \frac{X_1}{2} + nX \le r \le \frac{X_1}{2} + \frac{X_2}{2} + nX \end{cases} \tag{3.49}$$

where X_1 and X_2 are the two periods of the matter profile or potential, $X = X_1 + X_2$, and n is integer. The parametric resonance condition derived by E. Akhmedov [11]

is,

$$\frac{\tan(\omega_{\mathrm{m}1}X_1/2)}{\tan(\omega_{\mathrm{m}2}X_2/2)} = -\frac{\cos 2\theta_{\mathrm{m}2}}{\cos 2\theta_{\mathrm{m}1}}, \tag{3.50}$$

where $\omega_{\mathrm{m}i}$ and $\theta_{\mathrm{m}i}$ are the energy difference and mixing angle for potential Λ_1 and Λ_2 respectively.

Even though this castle wall problem is analytically solved, the resonance condition Eqn. (3.51) itself is not transparent. In this subsection, we show that such a system is closed related to Rabi oscillations. For illustration purpose, we set the profile to be equal period for the two densities so that $X_1 = X_2 \equiv X/2$. To show that the neutrino flavor conversions in this castle wall matter profiles is related to Rabi oscillation, we decompose the profile using Fourier series,

$$\lambda(r) = \lambda_0 + \sum_{n=1}^{\infty} \lambda_n \cos\left(k_n r\right), \tag{3.51}$$

where

$$\begin{aligned}
\lambda_0 &= (\Lambda_1 + \Lambda_2)/2, \\
\lambda_n &= \frac{2}{(2n-1)\pi}(-1)^n \left(\Lambda_1 - \Lambda_2\right), \\
k_n &= (2n-1)k_0, \\
k_0 &= 2\pi/X.
\end{aligned}$$

The decomposition is visualized in Fig. **??**.

To calculate the transitions between two mass states of background matter potential λ_0, we use the background matter basis with respect to λ_0, in which the transition is zero when varying matter profile vanishes. The Hamiltonian

$$\mathsf{H}^{(\mathrm{m})} = -\frac{1}{2}\omega_{\mathrm{m}}\sigma_3 + \frac{1}{2}\sum_{n=1}^{\infty}\lambda_n \cos 2\theta_{\mathrm{m}} \cos\left(k_n r\right)\sigma_3 - \frac{1}{2}\sum_{n=1}^{\infty}\lambda_n \sin 2\theta_{\mathrm{m}} \cos\left(k_n r\right)\sigma_1, \tag{3.52}$$

determines the transitions between the two background matter states.

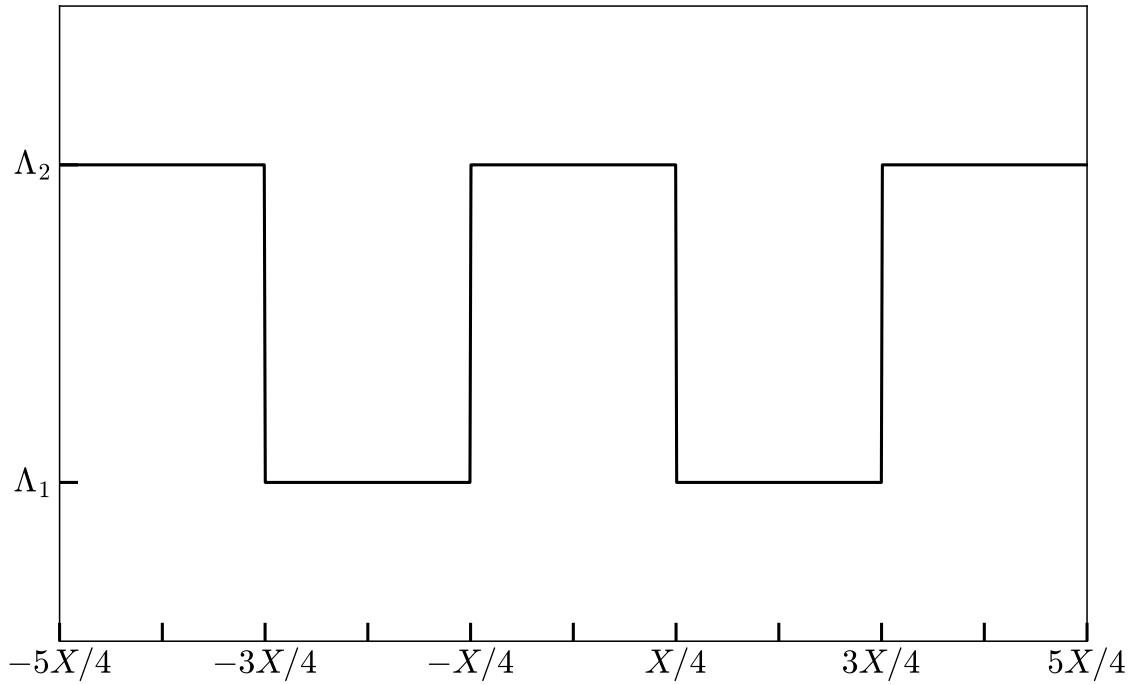

Figure 3.8: The castle wall matter potential profile with $X_1 = X_2 = X/2$. $\Lambda_2 = 0.7\omega_{\rm v}\cos 2\theta_{\rm v}$
$\Lambda_1 = 0.3\omega_{\rm v}\cos 2\theta_{\rm v}$

The base frequency k_0 which is determined by the total period X can be arbitrary. In this example, we choose a X so that the base frequency k_0 matches the energy gap $\omega_{\rm m}$. Even though multiple perturbation frequencies show up in Eqn. (3.53), we identify that only the first frequency $n = 1$ is the resonance frequency since we are using $k_0 = \omega_{\rm m}$. As an approximation, we drop all other frequencies $n > 2$ regarding the fact that they are far from resonance. Thus, similar to single frequency matter profile, the varying σ_3 terms have limited effects on the transition probabilities in

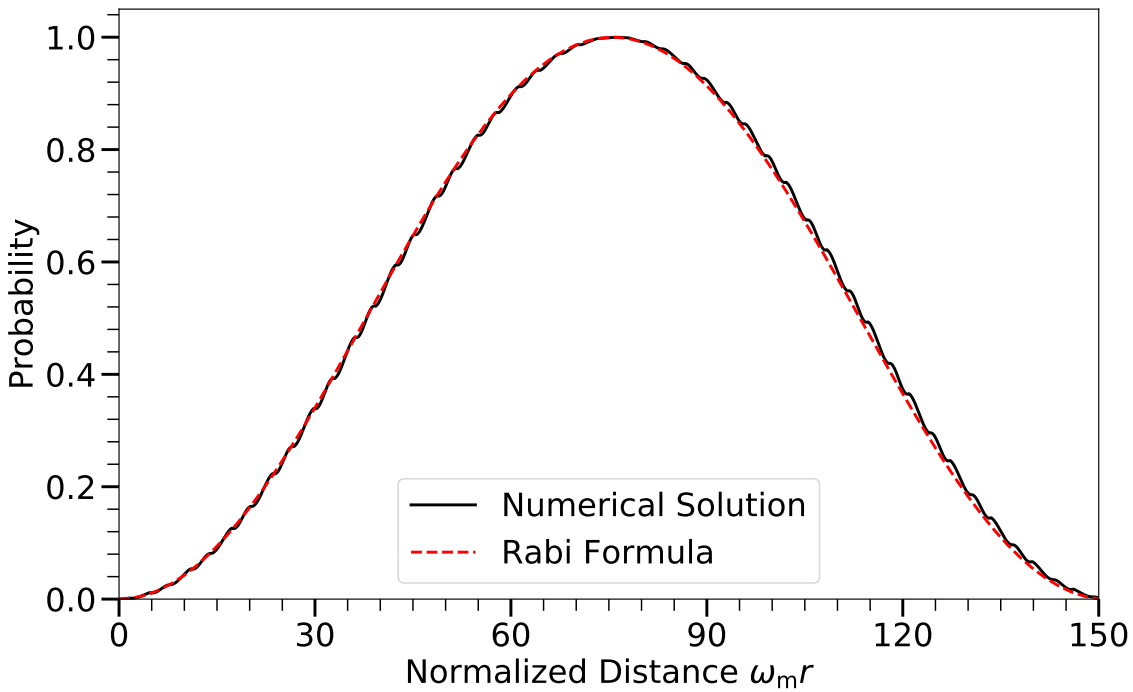

Figure 3.9: Transition probabilities for castle wall matter profile calculated numerically for $\Lambda_2 - \Lambda_1 = 0.4\Lambda_0$. During the calculation, the energy of neutrinos is 10 MeV, mass-squared difference is $\delta m^2 = 2.6 \times 10^{-3}\,\mathrm{eV}^2$, and the vacuum mixing angle chosen so that $\sin^2(2\theta_v) = 0.093$. The background potential Λ_0 is chosen so that it's half the MSW resonance potential, $\Lambda_0 = \frac{1}{2}\lambda_{\mathrm{MSW}} = \frac{1}{2}\omega_v \cos 2\theta_v$, and the base frequency is set to $k_0 = 2\pi/X = \omega_m$.

our case, which leads to

$$\begin{aligned}
\mathsf{H}^{(m)} &\to -\frac{1}{2}\omega_m\sigma_3 - \frac{1}{2}\sum_{n=1}^{2}\lambda_n \sin 2\theta_m \cos\left(k_n r\right)\sigma_1 \\
&\to -\frac{1}{2}\omega_m\sigma_3 - \frac{1}{2}\sum_{n=1}^{2} A_n \cos(k_n r)\sigma_1 \\
&\quad + \frac{1}{2}\sum_{n=1}^{2} A_n \sin(k_n r)\sigma_2,
\end{aligned}$$

where

$$A_n = \frac{\lambda_n \sin 2\theta_m}{2}.$$

The relative detuning is 0 if we have only the first mode. However, it becomes

$$D_1' = \frac{A_2^2}{2|A_1(\omega_{\rm m} - k_2)|}, \tag{3.53}$$

if we include the second frequency k_2. One feature of this Fourier series expanded matter profile Eqn. (3.52) is that the width of each frequency decreases as the order n increases while the detuning of each frequency increases. We calculate the relative detuning for each frequency

$$D_n = \frac{|k_n - \omega_{\rm m}|}{|\lambda_n \sin 2\theta_{\rm m}/2|} = \frac{2(n-1)(2n-1)\pi\omega_{\rm m}}{(\Lambda_2 - \Lambda_1)\sin 2\theta_{\rm m}} \tag{3.54}$$

which is quadratic in n and inversely proportional to $\Lambda_2 - \Lambda_1$. We find that all higher frequencies k_n for $n > 2$ have very large relative detunings. The neutrino transition probability between the two matter states is shown in Fig. 3.9, where we find the system has almost full transition.

A more rigorous treatment is to use Jacobi-Anger expansion and find the Rabi modes, where we find that the mode that corresponds to single frequency k_1 dominates and all other modes have little destruction effect on it. Quantitatively, higher orders leads to smaller width $B_{\{n_i\}}$ yet larger detuning $\sum_n nk_n - \omega_{\rm m}$, which renders a smaller effect on the resonance mode $\{1, 0\}$, since the effect is evaluated as Eqn. (**??**). Table 3.2 lists the first few smallest relative detunings of Fig. 3.9. The second column is the relative detuning of the corresponding mode, while the third column is the relative detuning of mode $\{1, 0\}$ with the energy gap shift effect of the corresponding mode.

3.5 Conclusions

The solar neutrinos behave very differently from lab experiments since the Sun provides a high matter density lab which can not be built on the Earth. What's even

$\{n_1, n_2\}$	D	$D'_{\{1,0\}}$
$\{1, 0\}$	0	-
$\{-1, 0\}$	48	1.0×10^{-2}
$\{0, 1\}$	1.5×10^{2}	1.1×10^{-3}
$\{2, 0\}$	2.4×10^{2}	2.0×10^{-4}

Table 3.2: Relative detuning of each frequency.

more exotic, in a supernova explosion, 10^{58} neutrinos are released from the proto-neutron star, which is of radius 10km, in a few seconds. The huge number density of neutrinos and large density of matter both change the neutrino oscillations dramatically. The matter effect in supernova is also much more complicated than MSW for solar neutrinos since the rich distribution of matter density and high speed motion. In addition to matter effect, neutrino neutrino interaction will be very efficient because of the high neutrino number density.

Apart from the emission of neutrinos from nuclear reactions of electron capture and positron emission in the solar interior, supernova environment also gives rise to Bremsstrahlung pair neutrino production, electron-positron neutrino pair production, which brings all three flavors and also anti-neutrinos into the spectra. However, even the with the presence of intensive interaction between neutrinos and the leptons and hardrons, which thermalize the neutrinos in the supernova core, the neutrino spectrum escaping from the supernova core is not completely Fermi-Dirac distribution. Nonetheless, it is possible to parametrize it using nominal Fermi-Dirac distribution,[14]

$$f(E) \propto \frac{E^2}{1 + \exp(E/kT - \mu)}. \tag{3.55}$$

Some numerical results show that there is a deviation from this Fermi-Dirac distribution [10, 13]. Meanwhile, Keil Mathias and Georg Raffelt showed that it is good enough to approximate the neutrino spectrum from supernova in Monte Carlo

simulations using the so called "alpha fit",

$$f(E) \propto E^{\alpha} \exp\left(-(\alpha+1)\frac{E}{\langle E\rangle}\right), \tag{3.56}$$

where $\langle E\rangle$ is the average energy, or the first moment of energy. The values from Monte Carlo simulations falls into the range $\alpha = 2.5 \sim 5$, which clearly shows the spectra are pinched. It's a hint that the detection of deviation from nominal Fermi-Dirac distribution will show evidence of core-collapse information.

Even though we understand solar neutrinos well, the neutrino oscillations of supernova explosions are not so to our complete knowledge. The flavor content is subject to the solution to the neutrino oscillations. Phenomena such as spectral split due to neutrino-neutrino interaction and matter effect reshape the neutrino spectra significantly. That being said, more research on supernova neutrinos, especially supernova neutrino oscillations is critical to understand supernova explosion mechanisms, as well as future observation of supernova neutrino data.

In conclusion, we have provided an interpretation for neutrino flavor conversion in fluctuating matter with the help of Rabi oscillations. The work provided two different points of view that is related to Rabi oscillations.

The first point of view was to interpret the neutrino flavor conversions in background matter basis. In this basis, matter density fluctuations will introduced a fluctuation part to the diagonal elements of the Hamiltonian, which means that the energy gap is fluctuating if we draw analogy between this Hamiltonian and the Hamiltonian of Rabi oscillations. For neutrino flavor conversions in a single frequency matter profile, the neutrino flavor oscillations becomes large when the matter fluctuation frequency is close to the energy gap, which is the resonance condition. We anticipated that the fluctuations of energy gap have limited effects on neutrino flavor conversions under this resonance condition. Thus the matter fluctuation only works as a pure flipping field that converts neutrinos from one flavor to another.

As we added more frequencies of matter density fluctuations, the neutrino flavor conversions becomes nontrivial due to the interferences between the difference matter profile frequencies. To quantify the interference between different Rabi oscillation modes, we defined relative detuning which describes how off-resonance a Rabi oscillation is. In the case of single frequency Rabi oscillations, the relative detuning becomes 0 under the resonance condition. As a second frequency is added to the oscillations, the energy gap is shifted due to this new frequency. A measure of the interference effect is to consider the relative detuning of the first frequency which is at resonance, under the shifted energy gap. Numerical results verified this conjecture. With the interference mechanism, we revisit the single frequency matter profile neutrino oscillations.

Another view is to switch to a basis where the neutrino oscillations Hamiltonian is decomposed into infinite Rabi oscillations. Equivalently speaking, the oscillations are consequences of superposition of Rabi oscillations, which we call modes of oscillations. This view was applied to emphasis the approximations that the change of energy gap due to matter fluctuation can be neglected under resonance condition in the previous background matter basis.

Chapter 4

Collective Neutrino Oscillations

Neutrino oscillations in the matter background has well defined linear dynamics as I discussed in the preceding chapters. However, the universe provides many other much more exciting labs for neutrino physics. One of such is supernova explosions, which release approximately 10^{58} neutrinos within seconds [6]. The neutrino density in supernova explosions could be dense enough for the neutrino self-interaction potential $H_{\nu\nu}$ to be comparable or even larger than the matter potential, depending on the region of interest in supernova explosions [4]. Thus self-interaction between neutrinos becomes non-negligible. Meanwhile, unexpected rich dynamics has been proved to exist with the self-interactions [21, 17]. The self-interactions introduce a new characteristic energy scale to neutrino oscillations, which makes it even possible to have matter-neutrino resonance [27, 32, 37].

In this chapter, I will review the neutrino collective oscillations and fast modes in neutrino collective oscillations. I will also review the connection between fast modes and dispersion relations proposed by I. Izaguirre et al [39]. Then I will show that the relation dispersion relations and fast modes is not well established. In the last few sections, I will discuss the neutrino halo problem, where scattering of neutrinos

is considered.

4.1 Collective Oscillations

4.1.1 Equation of Motion

The equation of motion for neutrino oscillations with self-interaction was first derived in [8]. For the purpose of the thesis, I will skip the quantum field theory derivations but write it down and clarify some conventions. The equation of motion is the Liouville's equation

$$\mathrm{i}\frac{d}{dt}\rho = [\mathsf{H}, \rho]. \tag{4.1}$$

For the purpose of vacuum neutrino oscillations, I have assumed that the neutrino travels with speed of light so that

$$\frac{d}{dt} = \frac{d}{dr}, \tag{4.2}$$

where r is the distance travelled by the neutrino. A more general approach is to rewrite the total derivative

$$\frac{d}{dt} = \partial_t + \mathbf{v}\cdot\boldsymbol{\nabla}. \tag{4.3}$$

On the right side, the Hamiltonian is composed of three different terms,

$$\mathsf{H} = \mathsf{H}_{\mathrm{v}} + \mathsf{H}_{\mathrm{m}} + \mathsf{H}_{\nu\nu}, \tag{4.4}$$

where H_{v}, H_{m} and H represents the vacuum Hamiltonian, matter Hamiltonian, and neutrino self-interaction Hamiltonian. Each of the three terms is explicitly written down

$$\mathsf{H}_{\mathrm{v}} = -\frac{1}{2}\beta\eta\omega_0\sigma_3 \tag{4.5}$$

$$\mathsf{H}_{\mathrm{m}} = \frac{1}{2}\sqrt{2}G_F n_e \sigma_3 \tag{4.6}$$

$$\mathsf{H}_{\nu\nu} = \sqrt{2}G_F \int d\omega d\Omega_{\hat{v}'} n(\omega, \hat{v}')\beta(\hat{v}')\rho(\omega, \hat{v}')(1 - \hat{v}\cdot\hat{v}'). \tag{4.7}$$

I use $\eta = \pm 1$ for Normal Hierarchy and Inverted Hierarchy respectively. I also use $\beta = 1$ for neutrinos and $\beta = -1$ for antineutrinos. In other words, the vacuum frequency is $\omega_{\rm v} = \eta\omega_0$. $\beta(\hat{v}')$ indicates whether the density matrix $\rho(\omega, \hat{v}')$ is for neutrinos or antineutrinos. If $\beta(\hat{v}') = -1$, $\rho(\omega, \hat{v}')$ is for antineutrinos, vice versa. More explicitly, the vacuum Hamiltonian is

$$\mathsf{H}_{\rm v} = \begin{cases} -\frac{1}{2}\eta\omega_{\rm v}\sigma_3 & \text{for neutrinos} \\ \frac{1}{2}\eta\omega_{\rm v}\sigma_3 & \text{for antineutrinos} \end{cases}$$

while the neutrino-neutrino interaction Hamiltonian is

$$\mathsf{H}_{\nu\nu} = \begin{cases} \sqrt{2}G_{\rm F}\int d\omega d\Omega_{\hat{v}'} n(\omega, \hat{v}')\rho(\omega, \hat{v}')(1 - \hat{v}\cdot\hat{v}') & \text{interacting with neutrinos} \\ -\sqrt{2}G_{\rm F}\int d\omega d\Omega_{\hat{v}'} n(\omega, \hat{v}')\bar{\rho}(\omega, \hat{v}')(1 - \hat{v}\cdot\hat{v}') & \text{interacting with antineutrinos} \end{cases}$$

Please note that I have used the following notation.

- $\omega_{\rm v}$ is the absolute value of the frequency, since η takes care of the signs;
- The integral in $\mathsf{H}_{\nu\nu}$ must take care of both interactions with neutrinos and anti-neutrinos.

I also use the following quantities in this chapter.

- λ is the same as the previous chapter

$$\lambda = \sqrt{2}G_{\rm F}n_{\rm e}. \tag{4.8}$$

- Angle distribution of number density is denoted as

$$f(\hat{v}) = \frac{n(\omega, \hat{v})}{n_{\rm t}}, \tag{4.9}$$

  where $n_{\rm total}$ is the total number density of neutrinos for all energies. It can also be defined for anti-neutrinos

$$\bar{f}(\hat{v}) = \frac{\bar{n}(\omega, \hat{v})}{\bar{n}_{\rm t}}, \tag{4.10}$$

where $\bar{n}_{\rm t}$ is the total number density of antineutrinos. One of the useful models is the line model, where neutrinos are emitted from a line. This model is a 2D neutrino problem. The direction of momentum $\hat{v}$ only depends on one angle, hence the distribution becomes $f(\theta)$. With this definition, the number density of neutrinos for some specific frequency ω within a range of angle $[\theta, \theta + d\theta]$ can be calculated using

$$n_{\rm t} f(\theta) d\theta. \tag{4.11}$$

Similarly, the the number density of antineutrinos within angle $[\theta, \theta + d\theta]$ is

$$\bar{n}_{\rm t} \bar{f}(\theta) d\theta. \tag{4.12}$$

- An asymmetry parameter can be defined to connect the total number density of neutrinos and antineutrinos,

$$\alpha = \frac{\bar{n}_{\rm t}}{n_{\rm t}}. \tag{4.13}$$

With the three definitions we simplify the neutrino self-interactions with matter effect

$$\begin{aligned}
\mathsf{H}_{\rm m} =& \frac{1}{2}\lambda\sigma_3 \\
\mathsf{H}_{\nu\nu} =& \sqrt{2} G_{\rm F} n_{\rm t} \int d\omega d\Omega_{\hat{v}'} f(\omega, \hat{v}) \rho(\omega, \hat{v}') (1 - \hat{v} \cdot \hat{v}') \\
& - \sqrt{2} G_{\rm F} \bar{n}_{\rm t} \int d\omega d\Omega_{\hat{v}'} \bar{f}(\omega, \hat{v}) \bar{\rho}(\omega, \hat{v}') (1 - \hat{v} \cdot \hat{v}') \\
=& \frac{1}{2}\mu \int d\omega d\Omega_{\hat{v}'} f(\omega, \hat{v}) \rho(\omega, \hat{v}') (1 - \hat{v} \cdot \hat{v}') \\
& - \frac{1}{2}\alpha\mu \int d\omega d\Omega_{\hat{v}'} \bar{f}(\omega, \hat{v}) \bar{\rho}(\omega, \hat{v}') (1 - \hat{v} \cdot \hat{v}'),
\end{aligned}$$

where

$$\mu = 2\sqrt{2} G_{\rm F} n_{\rm t}. \tag{4.14}$$

4.1.2 Synchronization in Neutrino Oscillations

With the equation of motion Eqn. 4.1, many aspects of such a system can be explored, such as neutrino bulb model, line model, etc. New dynamics, such as spectral split, synchronizations, matter-neutrino resonances, have been identified [17, 27, 32]. Synchronization is one of the most surprising results which might happen when neutrino number density is large.

To understand this phenomenon, I use the flavor isospin picture. Flavor isospin was explained in Sec. 2.4. Here we explain another definition of it

$$\rho = 1 + \vec{s} \cdot \vec{\sigma}. \tag{4.15}$$

For antineutrinos, the flavor isospin is defined as

$$\bar{\rho} = 1 - \vec{s} \cdot \vec{\sigma}. \tag{4.16}$$

The reason for the negative sign is that we usually reformulate the formula for antineutrinos and define the anti-neutrinos to have negative frequency.

With flavor isospin defined, to derive an equation for flavor isospin, we need to decompose the Hamiltonian into vectors. The vacuum and matter part is easy. It's straight forward to write down the vacuum part and matter part of Hamiltonian using three dimensional vectors in flavor isospin space,

$$\vec{H}_{\rm v} = \omega_{\rm v} \begin{pmatrix} -\sin 2\theta_{\rm v} \\ 0 \\ \cos 2\theta_{\rm v} \end{pmatrix}, \qquad \vec{H}_{\rm m} = \lambda \begin{pmatrix} 0 \\ 0 \\ -1 \end{pmatrix} \tag{4.17}$$

But the neutrino coherent scattering term requires some simplifications. For the purpose of the physics picture, we consider isotropic and homogeneous model which leads to

$$\vec{H}_{\nu\nu} = \sqrt{2} G_{\rm F} n_\nu \int d\vec{p}'^3 (1 - \vec{p} \cdot \vec{p}')(\rho_{\vec{p}'} - \bar{\rho}_{\vec{p}'}) = \sqrt{2} G_{\rm F} n_\nu \int dE' \frac{1}{n_\nu} (\rho_{E'} - \bar{\rho}_{E'}). \tag{4.18}$$

The flavor isospin will precess around $\vec{H}_{\nu\nu}$ assuming no vacuum or matter contributions.We have to define a vector, which is an integral of flavor-isospin vector over all energies or frequencies,

$$\vec{D} = \int d\omega' \vec{s}(\omega'). \tag{4.19}$$

Eqn. 4.18 becomes $\vec{H}_{\nu\nu} = \mu\vec{D}$, where $\mu = \sqrt{2}G_{\rm F}n_{\nu}$.

For single energy or flavor isospins aligned in the same direction, this vector is in the direction of the flavor isospin vector. If the flavor isospins are initially prepared in completely random and uniformly distributed directions, $\vec{D} \sim 0$.

Synchronization occurs when the neutrino number density becomes large. $\vec{D}$ will wobble around very fast due to the precessions of flavor isospins, but almost stays in one direction. All the spins precess with the same frequency which is determined by μ.

With vacuum contribution $\vec{H}_{\rm v}$ and matter contribution $\vec{H}_{\rm m}$ to the Hamiltonian, we expect $\vec{D}$ to precess around $\vec{H}_{\rm v} + H_{\rm v}$, if the precession frequency of flavor isospins around $\vec{D}$ is much larger than the precession frequency of $\vec{D}$ around $\vec{H}_{\rm v} + H_{\rm v}$.

Before we work out the solutions, the oscillation scale of collective oscillations can be estimated. The characteristic energy scale for vacuum oscillations is $\omega_{\rm v} = \delta m^2/2E$, while the characteristic energy scale for collective oscillations is $\mu \sim G_{\rm F}(1 - \hat{\boldsymbol{v}}_1 \cdot \hat{\boldsymbol{v}}_2)n_{\nu}$. Correspondingly, the vacuum oscillation frequency is

$$\begin{aligned}\omega_{\rm v} = \frac{\Delta m^2}{2E} \sim & \frac{2\pi}{1\text{km}} \left(\frac{\Delta m^2_{32}}{2.5 \times 10^{-3}\text{eV}^2}\right) \left(\frac{1MeV}{E}\right) \\ \sim & \frac{2\pi}{33\text{km}} \left(\frac{\Delta m^2_{12}}{7.5 \times 10^{-5}\text{eV}^2}\right) \left(\frac{1\text{MeV}}{E}\right)\end{aligned}$$

As for collective oscillations, suppose we have neutrino flux $10^{50}\text{ergs} \cdot \text{s}^{-1}$. We estimate the potential at radius R to be

$$\mu \sim \frac{1}{0.01km} \left(\frac{100\text{km}}{R}\right)^2 \left(\frac{1\text{MeV}}{E}\right),$$

which means that the collective oscillations frequencies in supernova explosions can be much smaller than vacuum oscillations.

4.2 Two Beams Model and Linear Stability Analysis

For nonlinear systems, linear stability analysis comes into play. I will go through the procedure and demonstrate the significance of instabilities and crossing in spectrum. For the sole purpose, I use a simple two-beam line model. The two beams model is simple mathematically, meanwhile reveals the key insights.

In this model, neutrinos are emitted in two different directions from a line which preserves translation symmetry on this line. The emission angles are shown in Fig. 4.1. For convenience of notations, I define a number density distribution function

$$f(\hat{v},\omega) = \frac{n(\hat{v},\omega)}{n_t}, \tag{4.20}$$

where n_t is the total number density of all neutrino emitted, $n(\hat{v},\omega)$ is the number density with momentum direction $\hat{v}$ and energy ω. We also define

$$\mu = \sqrt{2} G_{\rm F} n_t. \tag{4.21}$$

For two dimensional systems, we can calculate the neutrinos within an angle $[\theta, \theta+d\theta]$

$$n_t f(\hat{v},\omega) d\theta. \tag{4.22}$$

Similarly we can define the angular distribution for antineutrinos.

If all the beams are neutrinos, but with different energies for the left and right beams. The distribution function for beams is delta function. In fact, each beam is just half of the total neutrino number density n_t.

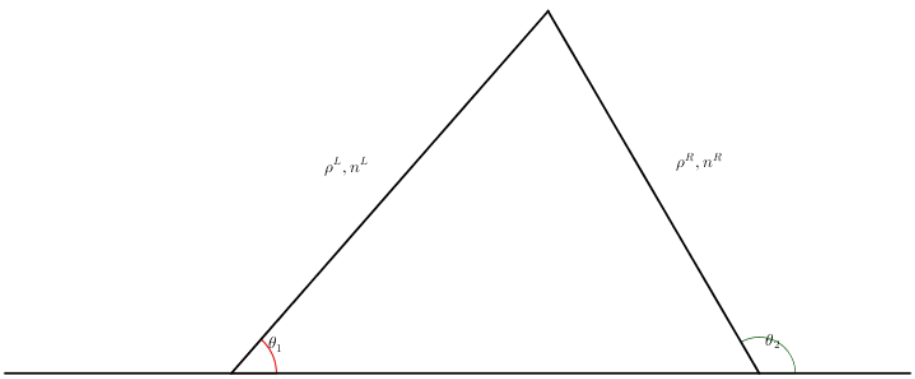

Figure 4.1: Geometry of two-beam model to be used in this section. Two neutrino beams are emitted, the states of which are denoted as ρ^L and ρ^R, with number densities n^L and n^R respectively. The emission angles are shown in the figure as θ_2 and θ_1 respectively.

The Hamiltonian is a sum of vacuum terms, matter terms, and self-interaction terms,

$$\mathsf{H} = \mathsf{H}_v + \mathsf{H}_m + \mathsf{H}_{\nu\nu}, \tag{4.23}$$

where

$$\mathsf{H}_{\mathrm{v}} = -\eta\frac{1}{2}\omega\sigma_3 \tag{4.24}$$

$$\mathsf{H}_{\mathrm{m}} = \frac{1}{2}\lambda\sigma_3 \tag{4.25}$$

$$\mathsf{H}^L_{\nu\nu} = \frac{1}{2}\mu^R\rho^R(1-\cos(\theta_1-\theta_2)) \tag{4.26}$$

$$\mathsf{H}^R_{\nu\nu} = \frac{1}{2}\mu^L\rho^L(1-\cos(\theta_1-\theta_2)). \tag{4.27}$$

To linearize the equation of motion, we define the perturbed density matrix as

$$\rho = \frac{1}{2}\begin{pmatrix} 1 & \epsilon \\ \epsilon^* & -1 \end{pmatrix}, \tag{4.28}$$

where we have removed the trace part because it is alway time independent.

The linearized equation of motion becomes

$$\mathrm{i}\partial_z \begin{pmatrix} \epsilon_1 \\ \epsilon_2 \end{pmatrix} = -i \begin{pmatrix} \cot\theta_1 \partial_x & 0 \\ 0 & \cot\theta_2 \partial_x \end{pmatrix} \begin{pmatrix} \epsilon_1 \\ \epsilon_2 \end{pmatrix} + \frac{1}{2} \begin{pmatrix} (\lambda + \mu_2 - \eta\omega_1 - \mu_2 \cos(\theta_1 - \theta_2))/\sin\theta_1 & -\mu_2(1 - \cos(\theta_1 - \theta_2))/\sin\theta_1 \\ -\mu_1(1 - \cos(\theta_1 - \theta_2))/\sin\theta_2 & (\lambda + \mu_1 - \eta\omega_2 - \mu_1 \cos(\theta_1 - \theta_2))/\sin\theta_2 \end{pmatrix} \begin{pmatrix} \epsilon_1 \\ \epsilon_2 \end{pmatrix}, \tag{4.29}$$

where

$$\begin{aligned} \mu_1 =& \sqrt{2} G_F n_{t,1} \\ \mu_2 =& \sqrt{2} G_F n_{t,2}. \end{aligned}$$

4.2.1 Left-right Symmetric Emission

We first consider a simple case, where $\theta_1 = \theta_2 \equiv \theta$, $\lambda = 0$, $\eta = 1$, and homogeneous in x direction. For simplicity we define

$$\begin{aligned} \mu =& \sqrt{2} G_F (n_1 + n_2) \\ \mu_i =& \mu \frac{n_i}{n_1 + n_2} \equiv \mu f_i \\ \xi =& 1 - \cos(\theta_1 - \theta_2) \\ \omega_i' =& \lambda - \eta\omega_i. \end{aligned}$$

I am aware that this is not a self-consistent example since $\theta_1 = \theta_2$ indicates that $\xi = 0$. As we will see, no instability is present in this case. However, we keep the term ξ because we need to analyze the effect of symmetry breaking. This example builds up a formalism.

The equation for perturbations becomes

$$i\partial_z \begin{pmatrix} \epsilon_1 \\ \epsilon_2 \end{pmatrix} = \frac{1}{2\sin\theta} \begin{pmatrix} \omega_1' + \mu f_2 \xi & -\mu f_2 \xi \\ -\mu f_1 \xi & \omega_2' + \mu f_1 \xi \end{pmatrix} \begin{pmatrix} \epsilon_1 \\ \epsilon_2 \end{pmatrix}. \tag{4.30}$$

Since μ is the most important energy scale in this problem, we scale all energies with it.

$$i\partial_{\hat{z}} \begin{pmatrix} \epsilon_1 \\ \epsilon_2 \end{pmatrix} = \frac{1}{2\sin\theta} \begin{pmatrix} \hat{\omega}_1' + f_2 \xi & -f_2 \xi \\ -f_1 \xi & \hat{\omega}_2' + f_1 \xi \end{pmatrix} \begin{pmatrix} \epsilon_1 \\ \epsilon_2 \end{pmatrix}, \tag{4.31}$$

where

$$\begin{aligned} \partial_{\hat{z}} =& \frac{d}{\mu dz} \\ \hat{\omega}_i' =& \frac{\omega_i'}{\mu}. \end{aligned}$$

The characteristic equation for this equation is

$$\left((\Omega - \hat{\omega}_1' - f_2\xi)(\Omega - \hat{\omega}_2' - f_1\xi) - f_1 f_2 \xi^2\right) = 0, \tag{4.32}$$

which is simplified to

$$(\Omega - \Omega_1)(\Omega - \Omega_2) - f_1 f_2 \xi^2 = 0,$$

where

$$\begin{aligned} \Omega_1 =& \hat{\omega}_1' + f_2\xi \\ \Omega_2 =& \hat{\omega}_2' + f_1\xi. \end{aligned}$$

Complete the square

$$(\Omega - (\Omega_1 + \Omega_2)/2)^2 = \frac{1}{4}(\Omega_1 - \Omega_2) + f_1 f_2 \xi^2.$$

The solution becomes

$$\Omega = \frac{1}{2}(\Omega_1 + \Omega_2) \pm \sqrt{(\Omega_1 - \Omega_2)^2/4 + f_1 f_2 \xi^2}. \tag{4.33}$$

The condition to have positive imaginary part is

$$(\Omega_1 - \Omega_2)^2 + 4f_1 f_2 \xi^2 < 0,$$

or

$$-2\sqrt{-f_1 f_2 \xi^2} < \Omega_1 - \Omega_2 < 2\sqrt{-f_1 f_2 \xi^2},$$

and $f_1 f_2 \xi^2 < 0$. Recall the meaning of f_i,

$$f_i = \frac{n_i}{n_1 + n_2},$$

instability requires that we have a spectrum crossing, i.e., n_1 and n_2 have different signs. Plug in the definitions of Ω_i,

$$-2\sqrt{-f_1 f_2 \xi^2} < \eta(-\omega_1 + \omega_2)/\mu + (f_2 - f_1)\xi < 2\sqrt{-f_1 f_2 \xi^2}.$$

From this we can infer

- $f_1 f_2$ has to be negative, which means we can NOT have instabilities with only neutrinos or antineutrinos with all the symmetries we assumed. This is crossing.
- $-\omega_1 + \omega_2 = 0$ will remove the instability. So we have to have both neutrinos and antineutrinos.
- $f_2 - f_1$, $\eta(\omega_2 - \omega_1)$, and μ set limit on each other.
- $\theta_1 = \theta_2 \equiv \theta$ removes the instability since it leads to $\xi = 0$. The emission has to be asymmetric in this simple two beams model. This is trivial since equal emission angle means the beams are not colliding.

Another way of understanding this equation is to think of it as the growth of the length of the vector $\vec{v} = (\epsilon_1, \epsilon_2)^T$. For an arbitrary matrix differential equation of the form

$$\partial_z \mathbf{v} = \mathbf{A}\mathbf{v},$$

we can always decompose the matrix $\mathbf{A}$ into symmetric part and skew-symmetric part

$$\mathbf{A} = \frac{1}{2}(\mathbf{A} + \mathbf{A}^T) + \frac{1}{2}(\mathbf{A} - \mathbf{A}^T) \equiv \mathbf{A}^+ + \mathbf{A}^-.$$

We can identify the effect of $f_1 - f_2$ but this is not particularly useful since we can not say anything about the eigenvalues of matrix $\mathbf{A}$ from the eigenvalues of matrix $\mathbf{A}^+$ and $\mathbf{A}^-$.

4.2.2 Breaking Symmetries

For a line model, the symmetries we have are

- Time translation symmetry;
- Translation symmetry along the line;
- Energy spectrum of the beams; One of particular interest is to have different neutrino spheres for different energies which can be investigated using two beam model.
- Number density of left and right beams;
- Angle of left and right beams;
- With and without matter.
- Similar to the discussion of varying matter potential, symmetries can be broken globally, i.e., distribution as a function of spacetime coordinates.

I will discuss some of the symmetries mentioned above.

Emission Angle Parity Symmetry

The emission angles change the value of $\xi = 1 - \cos(\theta_1 - \theta_2)$ as well as rescale the quantities by angle dependent factor $1/\sin\theta_i$.

To see the importance of angles, we can redefine some quantities

$$\begin{aligned}\omega_i'' =& \frac{\omega_i'}{\sin\theta_i} \\ f_1'' =& \frac{f_1}{\sin\theta_2} \\ f_2'' =& \frac{f_2}{\sin\theta_1}.\end{aligned}$$

The we will reach the same characteristic equation as Eqn. 4.32. So the angles serves as shift of energy gap and angular distribution.

The region of instability changes in a convoluted way. Given angles we can always write down the expression and find out.

- The criteria of existence of instability doesn't change.
- The region of instability changes.

Matter Effect

Including matter will define vacuum frequencies, ω_i', which is effectively just a shift of vacuum frequencies. In the symmetric emission case, $\omega_1' - \omega_2'$ is independent of matter effect. But breaking the emission symmetry generates the degeneracy,

$$\hat{\omega}_1'' - \hat{\omega}_2'' = (\lambda/\sin\theta_1 - \lambda/\sin\theta_2 + \eta(-\omega_1/\sin\theta_1 + \omega_2/\sin\theta_2))/\mu`. \tag{4.34}$$

We notice that very large matter density shift the region to very small μ.

However, matter effect is not always this simple. Suppose we have different matter potential for different beams, when they collide they would have built a different phase due to matter effect.

The inhomogeneous matter effect has been studied in [28]. It can excite high Fourier moments of flavor-isospin picture, which makes a lot of sense because it generates fine structure in the x direction. This might be integrated into LESA effect.

Translation Symmetry

Translation symmetry is better explained by introducing Fourier transform in x direction.

For each mode, a term that is proportional to Fourier mode index m. It only appears in diagonal elements, thus is effectively a shift of vacuum frequencies, thus energies of neutrinos.

For each Fourier mode

$$\begin{pmatrix} \epsilon_1 \\ \epsilon_2 \end{pmatrix} = \mathbf{Q}(\Omega, k) e^{-i(\Omega t - kx)},$$

where we set $\Omega = 0$.

First term in RHS of Eqn. 4.29 becomes

$$-i \begin{pmatrix} \cot\theta_1 \partial_x & 0 \\ 0 & \cot\theta_2 \partial_x \end{pmatrix} \begin{pmatrix} \epsilon_1 \\ \epsilon_2 \end{pmatrix} = k \begin{pmatrix} \cot\theta_1 & 0 \\ 0 & \cot\theta_2 \end{pmatrix} \begin{pmatrix} Q_1 \\ Q_2 \end{pmatrix}.$$

We now define $\hat{\omega}_i''$, so that

$$\hat{\omega}_{k,i}'' = \hat{\omega}_i'' + 2\hat{k}\cot\theta_i,$$

where $\hat{k} = k/\mu$.

The k term contributes to the difference between $\Omega_{k,i} \equiv \hat{\omega}''_{k,i} + f''_i \xi$.

We notice that instability criteria doesn't change. However, the regime of instability changes. We also know that the instability region is determined by

$$|\Delta\hat{\omega}''_{12} + 2\hat{k}(\cot\theta_1 - \cot\theta_2) + \Delta f''_{12}\xi| < \sqrt{-f_1 f_2 \xi^2}, \tag{4.35}$$

where $\Delta\hat{\omega}''_{12} = \hat{\omega}''_1 - \hat{\omega}''_2$. The instability region shift from

$$-\sqrt{-f''_1 f''_2 \xi^2} - \Delta f''_{12}\xi < (\Delta\omega''_{12} + 2k(\cot\theta_1 - \cot\theta_2))/\mu < \sqrt{-f''_1 f''_2 \xi^2} - \Delta f''_{12}\xi \tag{4.36}$$

If $|\Delta\omega''_{12} + 2k(\cot\theta_1 - \cot\theta_2)|$ becomes larger, the region of instability is shifted to larger μ, i.e., larger number density.

Number Density of Emission

A crossing is required to have instability, i.e., $-f''_1 f''_2 > 0$. Meanwhile the number density on the left and right have little effects on the existence of instability. It shifts the region of instability for μ.

Energy of Emission

Different energy of two beams will make sure $-\omega_1 + \omega_2 \neq 0$. It has no effects on the criteria but changes the μ region of instability.

General Solutions to Line Model

For completeness, we solve the general line model, c.f. Eqn. 4.29. We know that real symmetric matrix has only real eigenvalues, from which we infer that $\mu_1 = \mu_2$ and $\theta_1 = \theta_2$ removes the instability. For translation symmetric models, that is $\partial_x \to 0$, we have the eigenvalues

$$\Omega = \frac{1}{4}(A \pm B),$$

where

$$
\begin{aligned}
A =& -\eta\omega_1/\sin\theta_1 - \mu_2/\sin\theta_1 + \eta\omega_2/\sin\theta_2 + \mu_1\xi/\sin\theta_2 + \lambda(1/\sin\theta_1 + 1/\sin\theta_2) \\
B =& (-4[(\lambda-\eta\omega_1)(\lambda+\eta\omega_2) + (\lambda(\mu_1-\mu_2) - \eta(\mu_1\omega_1+\mu_2\omega_2))\xi]\sin\theta_1\sin\theta_2 \\
&+[(\lambda+\eta\omega_2+\mu_1\xi)\sin\theta_1 + (\lambda-\eta\omega_1-\mu_2\xi)\sin\theta_2]^2\big)^{1/2}/(\sin\theta_1\sin\theta_2) \\
\xi =& 1-\cos(\theta_1-\theta_2).
\end{aligned}
$$

For antineutrinos, I only need to change $\mu_i \to -\bar{\mu}_i$ and $\omega_i \to -\bar{\omega}_i$, where $\bar{\mu} = \sqrt{2}G_F\bar{n}_t$, so that the equation becomes

$$
\begin{aligned}
i\partial_z \begin{pmatrix} \epsilon_1 \\ \epsilon_2 \end{pmatrix} &= -i \begin{pmatrix} \cot\theta_1\partial_x & 0 \\ 0 & \cot\theta_2\partial_x \end{pmatrix} \begin{pmatrix} \epsilon_1 \\ \epsilon_2 \end{pmatrix} \\
&+ \frac{1}{2} \begin{pmatrix} (\lambda-\bar{\mu}_2+\eta\bar{\omega}_1+\bar{\mu}_2\cos(\theta_1-\theta_2))/\sin\theta_1 & \bar{\mu}_2(1-\cos(\theta_1-\theta_2))/\sin\theta_1 \\ \bar{\mu}_1(1-\cos(\theta_1-\theta_2))/\sin\theta_2 & (\lambda-\bar{\mu}_1+\eta\bar{\omega}_2+\bar{\mu}_1\cos(\theta_1-\theta_2))/\sin\theta_2 \end{pmatrix} \begin{pmatrix} \epsilon_1 \\ \epsilon_2 \end{pmatrix}
\end{aligned}
$$

Assume that the left beam is neutrino beam and the right beam is antineutrno beam. The linearized equation of motion becomes

$$
\begin{aligned}
i\partial_z \begin{pmatrix} \epsilon_1 \\ \epsilon_2 \end{pmatrix} &= -i \begin{pmatrix} \cot\theta_1\partial_x & 0 \\ 0 & \cot\theta_2\partial_x \end{pmatrix} \begin{pmatrix} \epsilon_1 \\ \epsilon_2 \end{pmatrix} \\
&+ \frac{1}{2} \begin{pmatrix} (\lambda-\bar{\mu}-2\eta\omega_1+\bar{\mu}\cos(\theta_1-\theta_2))/\sin\theta_1 & \bar{\mu}(1-\cos(\theta_1-\theta_2))/\sin\theta_1 \\ -\mu(1-\cos(\theta_1-\theta_2))/\sin\theta_2 & (\lambda+\mu+\eta\omega_2-\mu\cos(\theta_1-\theta_2))/\sin\theta_2 \end{pmatrix} \begin{pmatrix} \epsilon_1 \\ \epsilon_2 \end{pmatrix}
\end{aligned}
$$

4.3 Fast Mode

In a paper by Chakraborty et al [33], they showed that neutrino flavor instabilities can grow with a rate that is proportional to the neutrino density, which has much faster oscillation frequencies than vacuum oscillations. For such a fast growth to happen, the author considered head on colliding neutrino beams. The derivation is much similar to what has been shown in the previous section.

As an estimation, the frequencies of vacuum oscillation is

$$\begin{aligned}\omega_{\rm v} =& \frac{\Delta m^2}{2E} \\ \sim& 6.3\times10^{-3}{\rm m}^{-1}\frac{\Delta m^2_{32}}{2.5\times10^{-3}{\rm eV}^2}\frac{1MeV}{E} \\ \sim& 1.90\times10^{-4}{\rm m}^{-1}\frac{\delta m^2}{7.5\times10^{-5}{\rm eV}^2}\frac{1{\rm MeV}}{E},\end{aligned}$$

where E is the neutrino energy. The corresponding oscillation wavelength is simply give by

$$\begin{aligned}\lambda_{12} =& 2\pi/\omega_{12} \sim 1{\rm km} \\ \lambda_{32} =& 2\pi/\omega_{32} \sim 33.1{\rm km}.\end{aligned}$$

The fast modes instability grows with a rate proportional to the neutrino potential $\mu = \sqrt{2}G_F n_\nu$, which is very large in dense neutrino media. A large growth rate indicates a faster flavor transformation than vacuum oscillations.

4.3.1 Dispersion Relation of Neutrino Flavor Conversion

We consider two-flavor scenario ($\nu_{\rm e}$ and $\nu_{\rm x}$) of neutrino oscillations. We also assume that all neutrinos and antineutrinos are emitted as electron flavor. The flavor evolution of neutrino ensemble depends on flavor density matrices of neutrinos ρ and antineutrinos $\bar{\rho}$ with energy E, direction of velocity $\hat{\mathbf{v}}$,

$$\mathrm{i}(\partial_t + \mathbf{v}\cdot\nabla)\rho = [H, \rho_n]\,, \tag{4.37}$$

where H is the Hamiltonian for neutrino oscillations. In the context, Hamiltonian depends on three different contributions from vacuum oscillations $H_{\rm v}$, interactions with matter $H_{\rm m}$, and interactions with neutrinos themselves $H_{\nu\nu}$. In this work, we ignore vacuum and matter terms since the concentration is on fast neutrino oscillations, which would occur even without neutrino mass differences [33, 38]. In

order to calculate the neutrino self-interaction term $H_{\nu\nu}$, the distribution of neutrinos (antineutrinos) $f_{\nu_{\rm e}(\bar{\nu}_{\rm e})}(\hat{\mathbf{v}}, E)$ and $f_{\nu_{\rm x}(\bar{\nu}_{\rm x})}(\hat{\mathbf{v}}, E)$ is required, where E is the energy of neutrinos (antineutrinos). We have

$$H_{\nu\nu} = \sqrt{2}G_{\rm F}\iint \frac{{\rm d}\cos\theta'{\rm d}\phi'}{4\pi} v^{\mu}v'_{\mu}\int \frac{E'^2{\rm d}E'}{2\pi^2}\left((f'_{\nu_{\rm e}} - f'_{\nu_{\rm x}})\rho' - (f'_{\bar{\nu}_{\rm e}} - f'_{\bar{\nu}_{\rm x}})\bar{\rho}'\right), \quad (4.38)$$

where $v^{\mu} = (1, \sin\theta\cos\phi, \sin\theta\sin\phi, \cos\theta)^{\rm T}$ is the four velocity of (anti)neutrinos in our spherical coordinate system. Without vacuum contribution, the equation of motion for antineutrinos has the same form [21].

We follow the same assumption in reference [39] that the the distribution of ν_x and $\bar{\nu}_x$ are the same, namely $f_{\nu_{\rm x}}(\hat{\mathbf{v}}, E) - f_{\bar{\nu}_{\rm x}}(\hat{\mathbf{v}}, E) = 0$. In addition, we have the same definition of electron lepton number (ELN) of neutrinos travelling in direction $\hat{\mathbf{v}}$ [39],

$$G(\hat{\mathbf{v}}) = \sqrt{2}G_{\rm F}\int \frac{E'^2{\rm d}E'}{2\pi^2}(f_{\nu_{\rm e}}(\cos\theta', \phi', E') - f_{\bar{\nu}_{\rm e}}(\cos\theta', \phi', E')). \quad (4.39)$$

To perform linear stability analysis, we assume that the density matrix has the form

$$\rho = \bar{\rho} = \begin{pmatrix} 1 & \epsilon \\ \epsilon^* & 0 \end{pmatrix}, \quad (4.40)$$

where $|\epsilon| \ll 1$. As a result, the linearized equations of motion depends only on $G(\hat{\mathbf{v}})$ and $\hat{\mathbf{v}}$. We also assume that all neutrinos and antineutrinos undergo the same behavior in linear regime, $\epsilon = \tilde{\epsilon}e^{-{\rm i}(\Omega t - \mathbf{K}\cdot\mathbf{x})}$. Izaguirre, Raffelt, and Tamborra defined the polarization tensor [39],

$$\Pi^{\mu}{}_{\nu} = 1 + \int \frac{d\Omega}{4\pi} G(\theta, \phi)\frac{v^{\mu}v_{\nu}}{\omega - k\hat{\mathbf{k}}\cdot\hat{\mathbf{v}}}, \quad (4.41)$$

which defines the dispersion relation $\Pi^{\mu}{}_{\nu}a^{\nu} = 0$, with $a^{\nu} = \int \frac{d\cos\theta' d\phi'}{4\pi} G(\hat{\mathbf{v}}')v^{\nu}\tilde{\epsilon}$. We find the nontrivial solutions by setting [39],

$$\det\left(\Pi^{\mu}{}_{\nu}\right) = 0. \quad (4.42)$$

For simplicity, we consider axial symmetric neutrino emission so that Eq. (4.42) becomes

$$\det\left(\omega\mathrm{I}+\frac{1}{2}\begin{pmatrix} I_0 & 0 & 0 & -I_1 \\ 0 & -\frac{1}{2}(I_0-I_2) & 0 & 0 \\ 0 & 0 & -\frac{1}{2}(I_0-I_2) & 0 \\ I_1 & 0 & 0 & -I_2 \end{pmatrix}\right) = 0, \tag{4.43}$$

where $\mathbf{I}$ is the rank 4 identity matrix and

$$I_m = \int_{-1}^{1} du G(u) \frac{u^m}{1-(|k|/\omega)\,u}. \tag{4.44}$$

where we define $u = \cos\theta$. Eq. (4.43) is equivalent to the result in reference [26]. $|k|/\omega$ is defined as the refractive index n of the flavor wave. For spectrum $G(u)$ without zero values, the forbidden region is given by $1-(|k|/\omega)\,u \leq 0$.

The dispersion relations can be categorized into two different types by symmetries. To incorporate azimuthal symmetry, we define solutions related to the first and second element of a^ν ($\nu = 1, 2$) to be multi-azimuthal angle (MAA) solutions since they are the only solutions that depend on azimuthal angle ϕ. The other solutions which are related to $\nu = 0, 3$ are defined to be the multi-zenith angle (MZA) solutions. The MAA solution is related to symmetry breaking in azimuthal angle only, which is determined by

$$\omega = \frac{1}{4}(I_0 - I_2). \tag{4.45}$$

Similarly, the MZA solution is related to symmetry breaking in both azimuthal angle and zenith angle, which is

$$\omega = -\frac{1}{4}\left(I_0 - I_2 \pm \sqrt{(I_0+I_2-2I_1)(I_0+I_2+2I_1)}\right). \tag{4.46}$$

We denote the solution associated with + sign in Eq. (4.46) as MZA+, while the solution assocated with − sign as MZA-. The two solutions are connected to each other

in dispersion relations. In general, it doesn't provide physical insights to distingush the two branches of solutions since they are simply two branches of the solution.

The solutions to Eq. (4.45) and Eq. (4.46) are dispersion relations $D(\omega, \mathbf{k})$ for a chosen direction of $\hat{\mathbf{k}} = \hat{\mathbf{z}}$ with axial symmetric neutrino emission.

4.3.2 Instabilities and Gaps

In reference [39], the authors relate gaps in dispersion relation to instabilities of neutrino oscillations. In this section, we review the idea of correspondence between gaps and instabilities first. Then we show that this relation is not a solid theory that can be generalized to all cases.

We continue the discussion of axial symmetric neutrino emissions but with discretized zenith angles θ thus discretized u. Hence the ELN is independent of azimuth angle ϕ. For neutrino emission with 2 zenith angles, the ELN spectrum is

$$G(u) = \sum_{i=1}^{2} g_i \delta(u - u_i). \tag{4.47}$$

The MAA solution becomes an equation of hypobola for ω and k, which has asymptotes $\omega = k u_i$ for $i = 1, 2$. Meanwhile, hyperbola equation has two solutions of ω (k) for any given real k (ω). The solutions are either real which indicates stable solutions or complex which indicates exponential growth or decrease in linear regime. On the other hand, non-existence of real solutions of ω (k) for given real k (ω) is equivalent to gap in dispersion relation. Thus the equivalence of gap and instabilities is guaranteed in neutrino emission with two-zenith-angle emission. The numerical calculations is normalized using the maximium value in spectrum which is a convention we follow for all discrete emission calculations. Unit for ω and k can be determined once the exact spectrum is determined. Upper panels of Fig. 4.2 is reproduction of left panels of Fig. 1 in reference [39]. The dispersion relation is

shown as black lines. The real part ω_{R} is shown as red solid lines. $\omega_{\mathrm{R}} \pm \omega_{\mathrm{I}}$ are shown are red dashed lines, where ω_{I} is the imaginary part of ω.

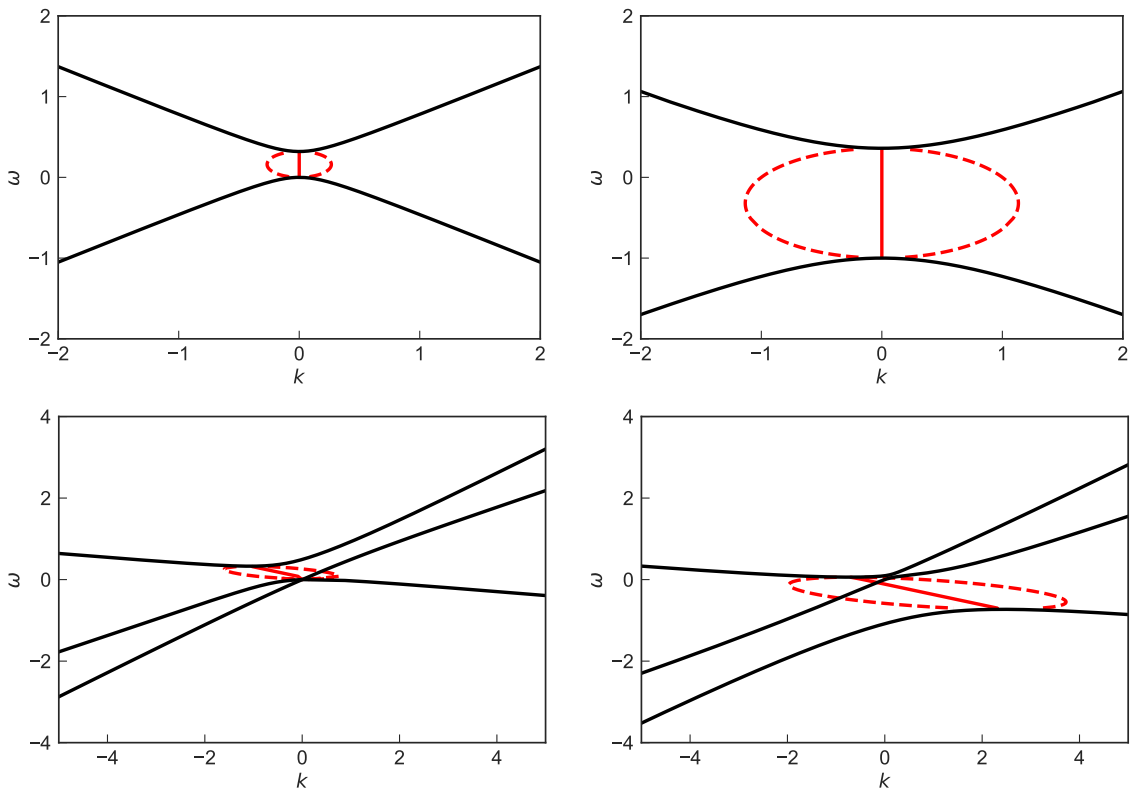

Figure 4.2: Dispersion relation and instabilities of two zenith angles spectrum (upper panels) and three zenith angles spectrum (lower panels). The black lines are the dispersion relations and the colored dots are examples of complex ω for real k. The left panels are the dispersion relation and linear stability analysis of MAA solutions while the right panels are for MZA solutions.

In core collapse supernova and neutron star mergers, neutrino emission is not in discrete zenith angles. More realistic models involve continuous zenith angle ELN spectra. In the case that the smooth and continuous ELN spectrum has no crossing, gap indeed indicates instabilities, as shown in reference [39]. In this section we prove that the instabilities in MAA, MZA+, or MZA- solution can only appear in either region $\omega \leq 0$ or region $\omega \geq 0$. As it suggests, the instability regions propagate

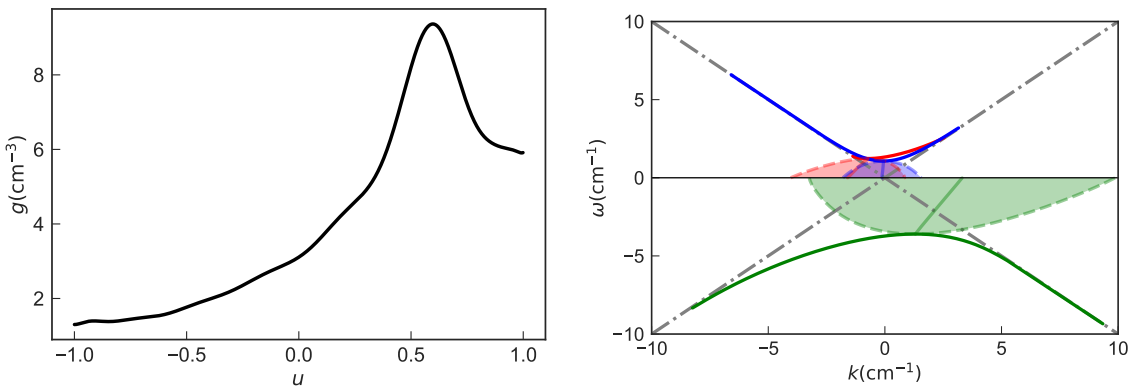

Figure 4.3: Dispersion relation and linear stability analysis (right panel) for a spectrum constructed from Garching 1D simulation data (left panel). Solid red line is dispersion relation for MAA solution while blue and green lines are for MZA solutions. Light red (green and green) blob is instability for MAA (MZA) solution.

only between the dispersion relation curves and the axis $\omega = 0$. We reproduced the calculation in reference [39] using the same Garching core-collapse supernova data set [42]. The spectrum shown in the left panel of Fig. 4.3 is polynomial fitting of the Garching 1D supernova simulation data. On the right of Fig. 4.3, the dispersion relation for MAA (MZA) solution is shown as red (green, blue) solid lines. Instabilities associated with MAA (MZA) solution is shown as light red (light green, light blue) blobs. The two branches of MZA solutions appear at the top half (MZA+) and lower half (MZA-). The result shows that instabilities occur either in region $\omega > 0$ or region $\omega < 0$ and with limits set the dispersion relation. We will prove that the instabilities appear between the dispersion relation and the axis $\omega = 0$.

Suppose we are looking for complex solutions for given real omega as in Fig. 4.3, MAA solution Eq. (4.45) is rewritten as a function $k(\omega/k)$. More explicitly, we have to solve the integral function to find out k for real ω,

$$k = \frac{1}{4}\int \mathrm{d}u G(u)\frac{1-u^2}{\omega/k - u}. \tag{4.48}$$

To investigate how instabilities developed around the horizental axies, we solve Eq. (4.48) in the limit $\omega \to 0$. For complex k, the integral can be decomposed into the principal value $\mathrm{Re}(k)$ and imaginary part $\mathrm{Im}(k)$ using Sokhotski–Plemelj theorem,

$$\mathrm{Re}(k) = \frac{1}{4}\left(\mathcal{P}\int \mathrm{d}u G(u)\frac{1-u^2}{-u}\right) \tag{4.49a}$$

$$\mathrm{Im}(k) = \frac{\pi}{4}G(0)\,\mathrm{Sign}\,(\omega)\,\mathrm{Sign}\,(\mathrm{Im}(k))\,. \tag{4.49b}$$

Assuming no crossing is found in sepctrum $G(u)$ at $u = 0$, Eq. (4.49b) shows that ω must have the same sign as $G(0)$ if we find nonzero imaginary part in k. We conclude that instabilities can only grow either in the upper plane $\omega > 0$ or lower plane $\omega < 0$. What's more, the value of k at limit $\omega \to 0$ can be solved out of Eq. (4.49a) and Eq. (4.49b). For instabilities the imaginary part of k tells us the growth rate is,

$$|\mathrm{Im}(k)| = \frac{\pi}{4}|G(0)|. \tag{4.50}$$

Similar result is obtained for MZA solutions,

$$\left(4\,\mathrm{Re}(k) - \mathcal{P}\int \frac{G(u)}{u}\mathrm{d}u + U_1\right)^2 - \left(\mathrm{Sign}(\omega\,\mathrm{Im}(k))\pi G(0) + 4\,\mathrm{Im}(k)\right)^2 \tag{4.51}$$

$$= -\left(\mathcal{P}\int \frac{G(u)}{u}\mathrm{d}u + U_1\right)\pi\,\mathrm{Sign}(\omega\,\mathrm{Im}(k))G(0), \tag{4.52}$$

where $U_m = \int G(u)u^m \mathrm{d}u$ and all the integrals are over all the sepctrum. The equations are quadratic in both $\mathrm{Re}(k)$ and $\mathrm{Im}(k)$ so the real solutions can be calculated and verified with linear stability analysis. The imaginary part $\mathrm{Im}(k)$

$$\mathrm{Im}(k) = -\frac{1}{4}\pi G(0)\,\mathrm{Sign}(\omega\,\mathrm{Im}(k))\left(1 \pm \frac{\mathscr{P}\int \frac{G(u)}{u}du + \int G(u)udu}{4\,\mathrm{Re}(k) - \mathscr{P}\int \frac{G(u)}{u}du + \int G(u)udu}\right) \tag{4.53}$$

determines that the two different solutions are either in the region $\omega > 0$ or in the region $\omega < 0$ which corresponds to MZA+ and MZA- solutions. The instabilities in the two regions are not continuous at $\omega = 0$.

4.3.3 Instabilities Do Not Always Show Up as Gap

Even though the concept of gap leads to instabilities works well for the models in 4.3.2, it can not be generalized to arbitrary number of emission angles nor to continuous spectra with crossings. As an example, we perform linear stability analysis of the three zenith angles emission configuration which is determined by a cubic function both in ω and k. Three solutions of $k(\omega)$ for given real $\omega(k)$ are expected. As long as real solutions disappear, complex solutions emerge, which leads to instabilities occur even without an actual gap. Rather the decrease in the number of real solutions for fixed ω or k corresponds to the instabilities. As an example, we plotted dispersion relation and instabilities for three zenith angles in lower panels of Fig. 4.2. For a given value of ω such as $\omega = 0.5$, the three MAA solutions (Fig. 4.2 lower left panel) of k are $k = -4.6, 0.29, 1.2$. All three solutions are all real and indicate no spatial instabilities which is confirmed by calculation of instabilities shown as red blob. However, for another real $\omega = 0.2$, we find only one real solution $k = 0.4$ from dispersion relation. The other solutions are complex and proven to be $k = -0.557106 \pm 0.966535\mathrm{i}$ where the value with positive imaginary part leads to exponential growth. We conclude that instabilities doesn't require gap in dispersion relation except for two emission angles.

We will prove that instabilities for continuous emission angles do not necessarily correspond to gap in dispersion relation. In the earlier works of fast modes, Sawyer analyzed a box shaped angular distribution of neutrino emission [36]. To address the generality of our conclusion, we repeat the calculation for box spectrum with crossing.

We construct a box spectrum with value -0.1 within $u \in [-1, -0.3)$ and value 1 within $[-0.3, 1]$ as shown in the top left panel of Fig. 4.4. As in the discrete emission case, we normalize all quantities using the maximium value of the spectrum. With

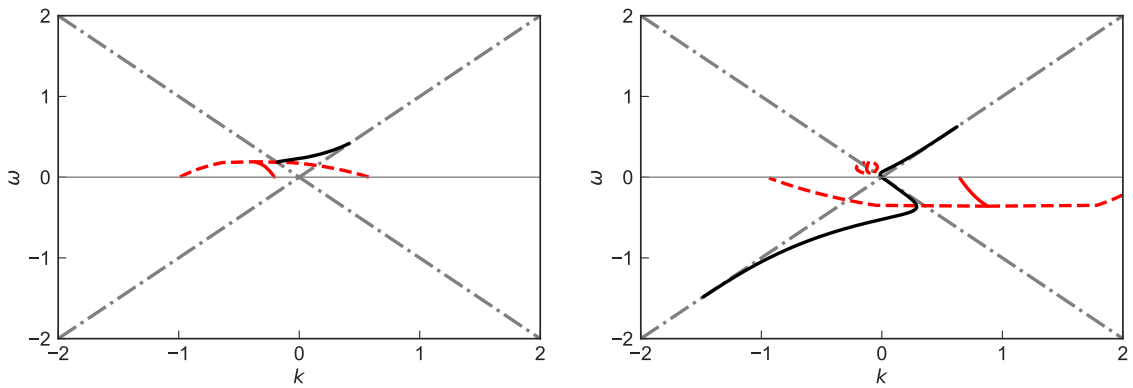

Figure 4.4: Dispersion relation and linear stability analysis for box spectrum. The box spectrum is defined to be -0.1 within range $u \in [-1, -0.3)$ and 1 within range $u \in [-0.3, 1]$. Left panel shows the dispersion relation and the complex k for real ω for MAA solution. Right panel is the corresponding result for MZA solution. Dash-dotted gray lines are $\omega = \pm k$ which sets the boundaries of the forbidden region for dispersion relation.

the spectrum defined, we calculate the dispersion relation and find out complex values of k for real ω. The result shows that the dispersion relation of both MAA solution and MZA solution contains only one curve. No gap is formed but we observe instabilities between this curve and $\omega = 0$ in MAA solution as well as two unstable regions of k in MZA solution, which are plotted as red lines.

4.4 Neutrino Halo Problem

One of the big questions about neutrino oscillations in supernovae is the so called halo problem. Cherry et al showed that neutrino flavor conversions are greatly affected by the back scattered neutrinos in supernovae [**Cherry2012**]. Neutrinos around supernovae are scattered and some of them are scattered to move almost backward. On the other hand, neutrino self-interactions is proportional to the inner product of momenta of neutrinos, which leads to the dependence on $1 - \cos\theta$ where θ is the

angles between momenta of two neutrinos. Most of the research has been concentrating on mostly forward scattering, with small values for $1 - \cos\theta$. For back ward scattered neutrinos, the interaction potential can be much larger than the forward scattered neutrino contributions. Though the work by Sarikas et al showed that matter suppression is still significant within this region [**Sarikas2012a**], it is not clear how exactly the neutrino halo alters neutrino oscillations. The halo problem itself is worth more calculations. In this chapter, I will present a relaxation method for this problem. The focus will be on the numerical method itself.

4.4.1 Line Model

We continue to use the simplified line model and build our intuitions out of it. The halo problem is simplified to have neutrinos emitted from a line $z = 0$ homogeneously, which are reflected from a certain distance $z = L$. In principle, the reflection angles doesn't have to be Snell's law. The scattering can be in any angle with different amplitudes. Here I am using this very simple Snell's law just to explore the effect of halo. It's crucial to keep an eye on the simplifications in this line model.

- Neutrinos are emitted from a line, which is not the case in a real supernova.
- Neutrinos are emitted with translation symmetry on the line. Breaking the symmetry might bring in other qualitatively different results.
- Neutrinos are reflected from a certain surface $z = L$, which is different from reality where neutrinos are scattered everywhere.
- Neutrinos are reflected according to Snell's law.
- Neutrinos are homogeneously reflected at $z = L$.

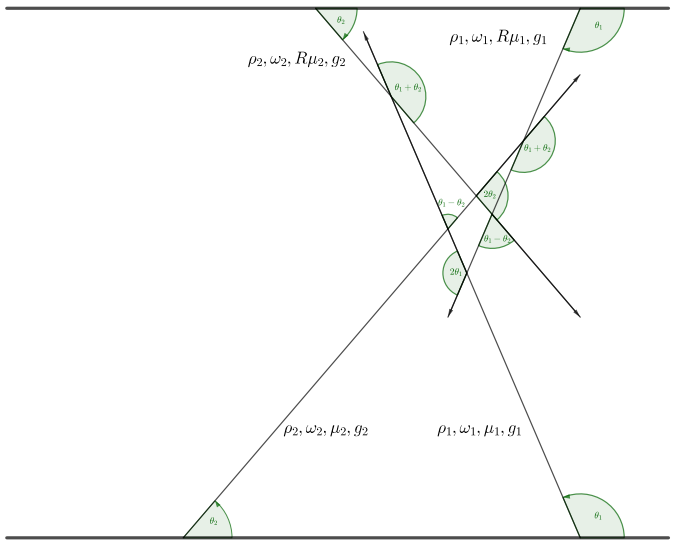

Figure 4.5: Line model used for halo problem. Neutrinos are emitted from the bottom line and reflected at the top line. Two neutrino beams are demonstrated in the figure. The beams are reflected from a surface at $z = L$.

The algorithm that I used is relaxation method. The algorithm is meant to find the equilibrium state of neutrino oscillations with the presence of halo.

1. Calculate forward beam using 0 backward beam;
2. Calculate backward beam using forward beam calculated in 1;
3. Calculate forward beam using backward beam calculated in 2;
4. Repeat until the beams reach equilibrium.

4.4.2 Neutrino Beams Only

As a first step, I calculated neutrino oscillations with only neutrino beams. Before we rush to the numerical results, I linearized the equation of motion and worked out

the linear stability analysis.

In linear regime, we define the density matrices for forward and backward beams to be

$$\rho_F = \frac{1}{2}\begin{pmatrix} 1 & \epsilon_F \\ \epsilon_B^* & -1 \end{pmatrix}$$
$$\rho_B = \frac{1}{2}\begin{pmatrix} 1 & \epsilon_B \\ \epsilon_B^* & -1 \end{pmatrix}.$$

The Hamiltonian for forward and back ward beams are

$$H_F = H_v + R\mu\rho_B$$
$$H_B = H_v + \mu\rho_F.$$

We will investigate the instability for zero mixing angle for new instabilities. The linearized equation of motion can be simplified to

$$i\partial_z \begin{pmatrix} \epsilon_F \\ \epsilon_B \end{pmatrix} = \begin{pmatrix} -\omega_v + R\xi\mu & -R\xi\mu \\ \xi\mu & \omega_v - \xi\mu \end{pmatrix} \begin{pmatrix} \epsilon_F \\ \epsilon_B \end{pmatrix}.$$

This equation can be easily solved. The eigenvalues are

$$\Omega_+ = \frac{1}{2}((R-1)\xi\mu + \sqrt{\Delta})$$
$$\Omega_- = \frac{1}{2}((R-1)\xi\mu - \sqrt{\Delta}),$$

where

$$\Delta = (1-R)^2\mu^2\xi^2 - 4\mu\xi\omega_v(1+R) + 4\omega_v^2. \tag{4.54}$$

The corresponding eigenvectors are

$$V_+ = \begin{pmatrix} \frac{-2\omega_v + \xi\mu(1+R) + \sqrt{\Delta}}{2\xi\mu} \\ 1 \end{pmatrix}$$
$$V_- = \begin{pmatrix} \frac{-2\omega_v + \xi\mu(1+R) - \sqrt{\Delta}}{2\xi\mu} \\ 1 \end{pmatrix}.$$

The general solution to the equation is

$$\begin{pmatrix} \epsilon_F(z) \\ \epsilon_B(z) \end{pmatrix} = C_+ V_+ e^{-i\Omega_+ z} + C_- V_- e^{-i\Omega_- z}.$$

The special property about this reflection problem is that the density matrices for the forward and backward beams should be the same at the reflection point, say $z = L$. With such a simple relation, we can find the relations between $C_\pm$ by setting $\epsilon_F(L) = \epsilon_B(L)$,

$$\frac{C_+}{C_-} = e^{-i(\Omega_- - \Omega_+)L} \frac{\sqrt{\Delta} + 2\omega_v + \mu\xi(1-R)}{\sqrt{\Delta} - 2\omega_v - \mu\xi(1-R)}. \tag{4.55}$$

The solution to be problem can be simplified,

$$\begin{pmatrix} \epsilon_F(z) \\ \epsilon_B(z) \end{pmatrix} = C_- e^{-i\Omega_- L} \left(\frac{\sqrt{\Delta} + 2\omega_v + \mu\xi(1-R)}{\sqrt{\Delta} - 2\omega_v - \mu\xi(1-R)} V_+ e^{-i\Omega_+(z-L)} + V_- e^{-i\Omega_-(z-L)} \right). \tag{4.56}$$

We are interested in the absolute values of each elements so that the overall factors can be neglected. The forward beam evolution is obtained by taking the absolute value of ϵ_F,

$$\begin{aligned} |\epsilon_F| \propto & |(2\omega_v + \xi\mu(1-R) + i\delta)(-2\omega_v + \xi\mu(1+R) + i\delta)e^{\delta(z-L)} \\ & + (-2\omega_v - \xi\mu(1-R) + i\delta)(-2\omega_v + \xi\mu(1+R) - i\delta)e^{-\delta(z-L)}|, \end{aligned}$$

in which $\sqrt{\Delta}$ is replaced by $i\delta$. We collecting terms and verify that it has the form

$$|\epsilon_F| \propto A + B\cosh(2\delta(L-z)), \tag{4.57}$$

where $B \leq 0$. The only z dependent term is $\cosh(2\delta(L-z))$, which is decreasing within $[0, L]$ and is increasing in $[L, 2L]$. The slope at $z = L$ is 0. An example is plotted in Fig. 4.6.

We expect the numerical calculations bare the same behavior that the instability leads to no growth but decrease in flavor conversion, assuming the neutrinos start from electron flavor. The result indeed confirms it. Fig. 4.7 is an example of it.

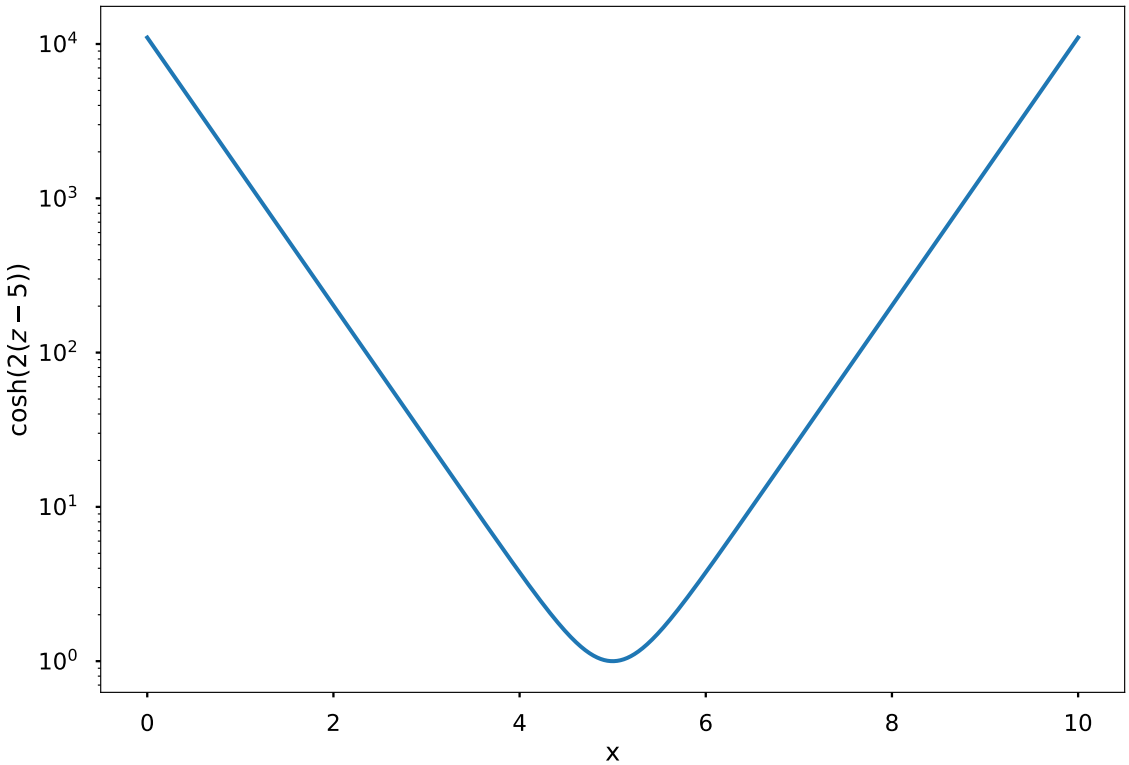

Figure 4.6: An example of $\cosh(2\delta(z-L))$ with $\delta = 1$, and $L = 5$. This function always reach the minimium at $z = L$.

For linear stability analysis, we usually identify real characteristic values of the linearized equation of motion. In bipolar model as explained in Sec. **??**, real characteristic values of the equation of motion indicates exponential growth, while it always indicates exponential decrease in this simplified halo problem.

We expect that only normal hierarchy has an instability region which is trivial since we noticed that the backward beam is acting like antineutrino beams but with different hierarchies.

$$i\partial_t \mathbf{s}_F = \mathbf{s}_F \times (\mathbf{H}_v + R\mu\mathbf{s}_B) \tag{4.58}$$

$$i\partial_t \mathbf{s}_B = \mathbf{s}_B \times (-\mathbf{H}_v - \mu\mathbf{s}_F). \tag{4.59}$$

Compare to Eq. **??**, we notice that the reflected beam works as an antineutrino beam

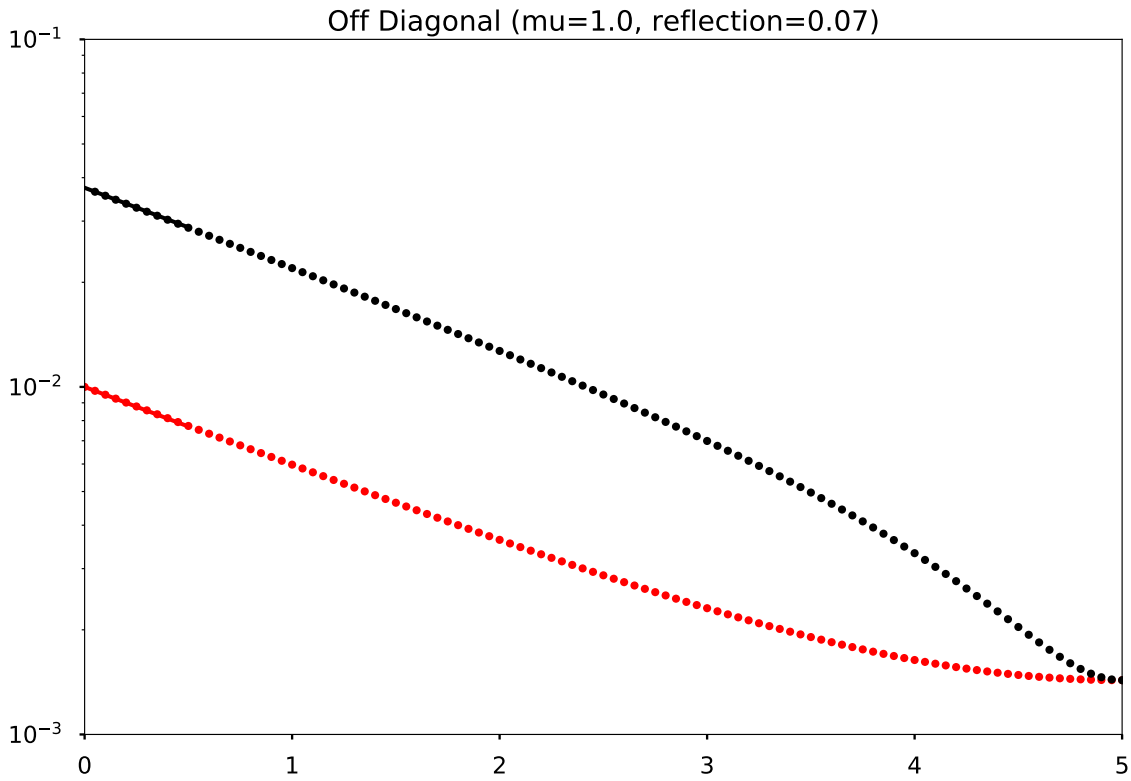

Figure 4.7: Absolute value of off diagonal element for $\mu = 1.0$, $R = 0.07$, $L = 5$, with normal hierarchy. The red dots are for the forward beam and the black dots are for the backward beams. The lines are indicating the predictions of linear stability analysis.

but the system becomes the opposite hierarchy compared to bipolar model. We find the instability regions in Fig. 4.8.

4.4.3 Two Beams Model with Reflection

The model is naturally extended to a two beams model including both neutrinos and antineutrinos. The configuration is exactly the same as shown in Fig. 4.5.

As the first step we work out the linear stability analysis. The four equations of

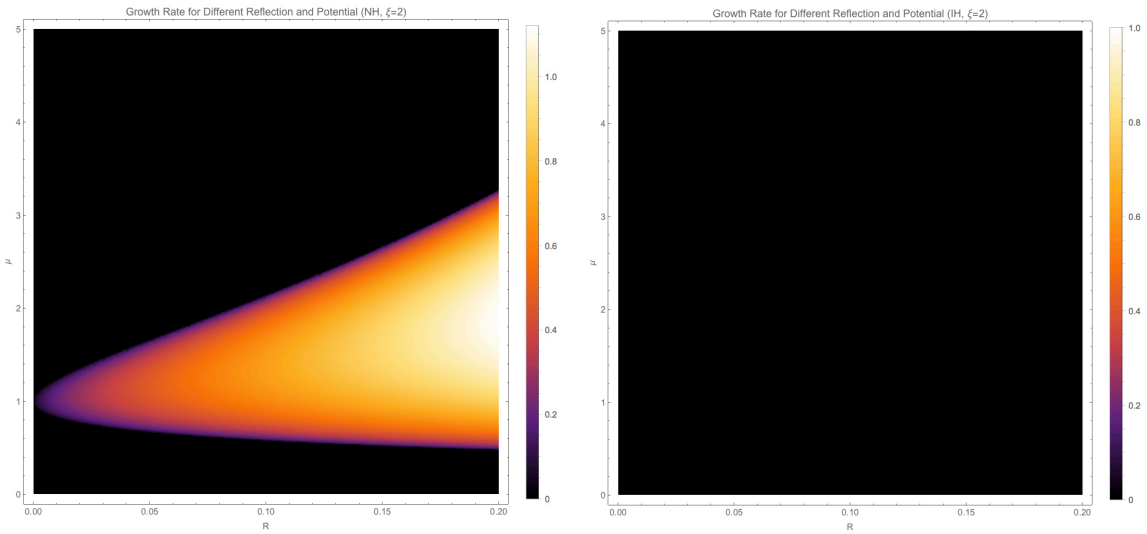

Figure 4.8: Instability regions for normal hierarchy (left) and inverted hierarchy (right) as a function of neutrino potential μ and reflection coefficient R, with vacuum mixing angle set to 0. No instabilities is found in inverted hierarchy.

motion are

$$i\partial_z\rho_1 = [H_1, \rho_1], \tag{4.60}$$

$$i\partial_z\rho_2 = [H_2, \rho_2], \tag{4.61}$$

$$-i\partial_z\rho_3 = [H_3, \rho_3], \tag{4.62}$$

$$-i\partial_z\rho_4 = [H_4, \rho_4], \tag{4.63}$$

where $_1$ and $_2$ are the quantities for two forward beams while $_3$ and $_4$ are the quantities for the corresponding backward going beams. For the purpose of this analysis we set $\theta_v = 0$. The Hamiltonians are

$$H_1 = -\eta\omega_v\sigma_3 + g_2\chi_-\mu_2\rho_2 + g_2\chi_+R\mu_2\rho_4 + g_1\chi_1R\mu_1\rho_3, \tag{4.64}$$

$$H_2 = \eta\omega_v\sigma_3 + g_1\chi_-\mu_1\rho_1 + g_2\chi_2R\mu_2\rho_4 + g_1\chi_+R\mu_1\rho_3, \tag{4.65}$$

$$H_3 = -\eta\omega_v\sigma_3 + Rg_2\chi_-\mu_2\rho_4 + g_2\chi_+\mu_2\rho_2 + g_1\chi_1\mu_1\rho_1, \tag{4.66}$$

$$H_4 = \eta\omega_v\sigma_3 + Rg_1\mu_1\chi_-\rho_3 + g_1\chi_+\mu_1\rho_1 + g_2\chi_2\mu_2\rho_2. \tag{4.67}$$

I have defined

$$\begin{aligned}\chi_+ =& 1 - \cos(\theta_1 + \theta_2),\\ \chi_- =& 1 - \cos(\theta_1 - \theta_2),\\ \chi_1 =& 1 - \cos(2\theta_1),\\ \chi_2 =& 1 - \cos(2\theta_2),\end{aligned}$$

and g_i represents the energy spectrum of the neutrinos and η stands for the hierarchy.

4.5 Relaxation Method for Neutrino Halo Problem

We choose a relaxation method scheme to solve this non-local boundary value problem numerically. To begin with, we write down the discretization scheme.

$$\rho(t + \Delta t) = \left[\cos(2h\Delta t)\rho_n - 2u_i\rho_i u_n\right]\sigma_n \tag{4.68}$$

$$= \left[\cos(2h\Delta t)\rho_n + 2\sin^2(h\Delta t)u_i'\rho_i u_n'\right]\sigma_n \tag{4.69}$$

The reason that we use fixed step size for this problem is that it's easier to calculate the neutrino self-interactions on such fixed grids. The algorithm is described as

1. Calculate forward beam using 0 backward beam;
2. Calculate backward beam and forward beam together using the state of beams from the previous step current counter beams;
3. Repeat the previous step until the state of the beams reach equilibrium.

To speed up the calculations, I also implemented OpenMP for parallel computing. The code is tested using vacuum oscillations (shown in Fig. 4.9) and bipolar models.

The reason that we still have conversions is because of the vacuum term, which is additional to linear stability analysis. It is also proven to reach equilibrium quickly as shown in Fig. 4.10.

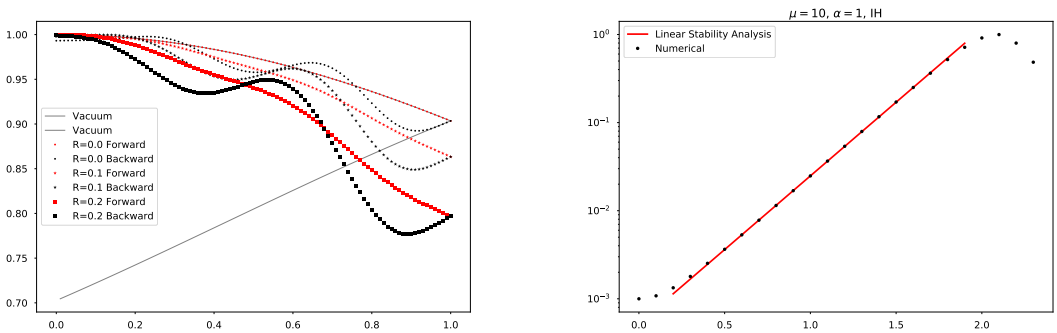

Figure 4.9: The left panel validates code by setting reflection to zero and approach vacuum for single forward beam. Meanwhile, we notice that for nonzero reflections, more conversion is done, which makes sense due to the similarity between R and the asymmetry parameter α in bipolar model. The right panel validates the code by setting reflection to zero and compare with bipolar model for two beams case, where the slope is matching the theoretical value 3.85.

4.6 Conclusion

The dispersion relations can be extracted from the linearized form of the equation of motion for collective neutrino oscillations. The dispersion relation becomes quadratic for neutrino emission with two zenith angles. Thus two solutions should be found for ω and k. The dispersion relations are hyperbolas and the gaps between the lines corresponds to instabilities. However, this correspondence doesn't hold for neutrinos emitted from more zenith angles. For more realistic spectrum, I have proved that instabilities propagate in regions of either $\omega > 0$ or $\omega < 0$ and never cross $\omega = 0$. Hence the dispersion relation gaps should be defined as gaps between the dispersion relation curves and the axis $\omega = 0$ instead of the dispersion relation curves. I

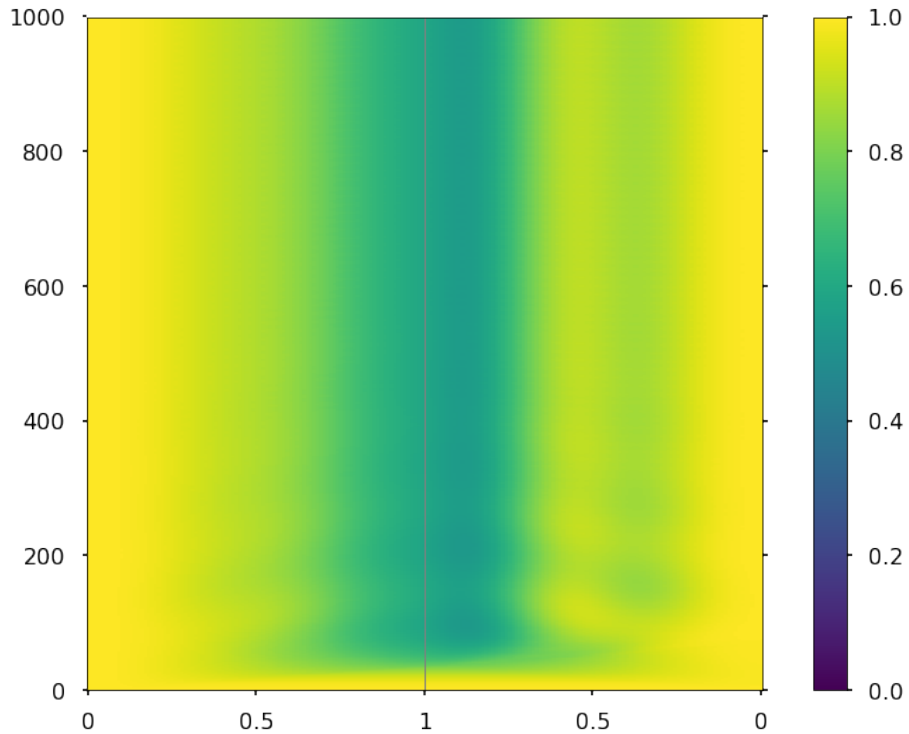

Figure 4.10: Relaxation method reaches equilibrium after some steps. The horizontal axis is the z direction while the vertical axis is the number of iteration steps. The color indicates the survival probability for electron flavor. This calculation sets $\mu = 4$, $R = 0.2$, and is done within range $[0, 1]$. Equilibrium is reached around step 400 and the neutrino states stays in equilibrium.

have also showed that instabilities is not necessarily shown as gap in dispersion relations for neutrino emission with more than two zenith angles and box spectrum with crossing. Through the discussions, I demonstrated that the relation between dispersion relation gaps and instabilities should be used with caution.

The second problem discussed in this chapter is the halo problem, which brings in more complexities to the neutrino oscillations. In the spirit of numerical methods, I developed a parallelable relaxation method, using C++ and OpenMP. Both the analytical and numerical results showed that for the two realms, either single forward beam or two forward beams, the results are compared with bipolar model. This

simple model is very similar to the bipolar model thus I can perform linear stability analysis and verify my numerical method. The reflection indeed may enhance the flavor conversions but it is not a new type of instability. Future work should be done to explore the effect of symmetry breaking and multiple emission beams.

Chapter 5

Conclusion

The neutrino is a common product in astrophysical environments which makes neutrino physics a key ingredient of astrophysics. Since different neutrino flavors have different impact on the dynamics of astrophysical objects, identifying the flavor dynamics of the neutrino becomes important. One the other hand, the neutrino converts between different flavors while it propagates due to the mismatch of flavor states and mass states. Thus the neutrino doesn't maintain its flavor as produced. Even more, the conversions are altered by neutrino interactions with the matter or the neutrino itself.

The interactions with matter lead to the so called MSW effect where neutrinos may experience maximum flavor conversion for some specific matter density. In this dissertation, I have also explained the neutrino parametric oscillations where the varying matter profile serves as the driving field for the neutrino two-level quantum system. The matter profile drives the neutrino oscillations to resonance when the frequency of the driving potential matches the energy gap of the two energy levels, which is quite similar to Rabi oscillations. However, the matter potential provides more than one driving frequencies. Those different driving frequencies interfere with

each other, which indicates that a second driving potential might lead to destruction of resonances of the original driving potential. This has been proved in the dissertation. I also prove that the interference might also enhance the resonance. The Rabi oscillations point of view has provided a simple picture to understand the neutrino oscillations in oscillatory matter profile.

For future research, neutrino oscillations in more realistic matter profile has to be calculated to locate the possible resonances. For example, the matter density in supernovae is Kolmogorov-like. To understand the matter effect on neutrino oscillations in supernovae, the possible resonances can be identified using the resonance condition and the interference effect. As for applications of this parametric resonance, one of them is neutrino tomography. Using resonances of neutrino oscillations at different energies, it is possible to infer the interior structure of celestial objects.

As for neutrino oscillations with self-interactions, the equation of motion can be linearized for linear stability analysis in this dissertation. Linear stability analysis is a very useful tool for neutrino oscillations in dense neutrino media. It reveals whether the neutrino will be converted to other flavors. While linear stability analysis has been used frequently in the research, I. Izaguirre et al. has concluded in [39] that the dispersion relations of neutrino oscillations can be defined and they correspond to flavor instabilities. The idea may sound pretty but I showed in this dissertation that dispersion relations gaps and flavor instabilities are not simply related. Flavor instabilities do not always exist within gaps of dispersion relations. They exist even when no gaps are found in the dispersion relations. I also talked about the so called neutrino halo problem in this dissertation. The supernova neutrinos are scattered when they are propagating.

Bibliography

[1] C L Cowan et al. “Detection of the Free Neutrino: a Confirmation.” In: *Science (New York, N.Y.)* 124.3212 (July 1956), pp. 103–4.

[2] B Pontecorvo. “Neutrino experiments and the problem of conservation of leptonic charge”. In: *Sov. Phys. JETP* 26.5 (1968), pp. 984–988.

[3] J.N. Bahcall. “The solar neutrino problem”. In: *Nuclear Instruments and Methods* 110 (July 1973), pp. 381–384.

[4] Elliott G Flowers and Peter G Sutherland. “Neutrino-neutrino scattering and supernovae”. In: *The Astrophysical Journal* 208.1 (Aug. 1976), p. L19.

[5] L. Wolfenstein. “Neutrino oscillations in matter”. In: *Physical Review D* 17.9 (May 1978), pp. 2369–2374.

[6] J. N. Bahcall, A. Dar, and T. Piran. “Neutrinos from the recent LMC supernova”. In: *Nature* 326.6109 (Mar. 1987), pp. 135–136.

[7] P.I. Krastev and A.Yu. Smirnov. “Parametric effects in neutrino oscillations”. In: *Physics Letters B* 226.3-4 (Aug. 1989), pp. 341–346.

[8] G. Sigl and G. Raffelt. “General kinetic description of relativistic mixed neutrinos”. In: *Nuclear Physics B* 406.1-2 (Sept. 1993), pp. 423–451.

[9] F. N. Loreti and A. B. Balantekin. “Neutrino oscillations in noisy media”. In: *Physical Review D* 50.8 (Oct. 1994), pp. 4762–4770. arXiv: `9406003 [nucl-th]`.

[10] T. Totani et al. "Future Detection of Supernova Neutrino Burst and Explosion Mechanism". In: *The Astrophysical Journal* 496.1 (Mar. 1998), pp. 216–225.

[11] E. Kh Akhmedov. "Parametric resonance in neutrino oscillations in matter". In: *Pramana* 54.1 (Jan. 2000), pp. 47–63. arXiv: `9907435 [hep-ph]`.

[12] Michael F Altmann, Rudolf L Mößbauer, and Lothar J N Oberauer. "Solar neutrinos". In: *Reports on Progress in Physics* 64.1 (Jan. 2001), pp. 97–146.

[13] Mathias Th. Keil. "Supernova Neutrino Spectra and Applications to Flavor Oscillations". PhD thesis. 2003. arXiv: `0308228 [astro-ph]`.

[14] Georg G. Raffelt et al. "Supernova neutrinos: Flavor-dependent fluxes and spectra". In: *Neutrino oscillations and their origin. Proceedings, 4th International Workshop, NOON2003, Kanazawa, Japan, February 10-14, 2003*. 2003, pp. 380–387. arXiv: `astro-ph/0303226 [astro-ph]`.

[15] Huaiyu Duan, George M. Fuller, and Yong-Zhong Qian. "Analysis of collective neutrino flavor transformation in supernovae". In: *Physical Review D* 74.12 (Dec. 2006), p. 123004. arXiv: `0703776 [astro-ph]`.

[16] Huaiyu Duan, George M. Fuller, and Yong-Zhong Qian. "Collective neutrino flavor transformation in supernovae". In: *Physical Review D* 74.12 (Dec. 2006), p. 123004. arXiv: `0703776 [astro-ph]`.

[17] Huaiyu Duan et al. "Simulation of coherent nonlinear neutrino flavor transformation in the supernova environment: Correlated neutrino trajectories". In: *Physical Review D - Particles, Fields, Gravitation and Cosmology* 74 (2006), pp. 1–22. arXiv: `0606616 [astro-ph]`.

[18] Alexander Friedland and Andrei Gruzinov. "Neutrino signatures of supernova turbulence". July 2006.

[19] R. W. Boyd. *Nonlinear Optics*. Third. Elsevier, 2008. ISBN: 978-0-12-369470-6.

[20] I. Ploumistakis, S.D. Moustaizis, and I. Tsohantjis. "Towards laser based improved experimental schemes for multiphoton pair production from vacuum". In: *Physics Letters A* 373.32 (2009), pp. 2897–2900.

[21] Huaiyu Duan, George M. Fuller, and Yong-Zhong Qian. "Collective Neutrino Oscillations". In: *Annual Review of Nuclear and Particle Science* 60.1 (Nov. 2010), pp. 569–594. arXiv: 1001.2799.

[22] James Kneller and Cristina Volpe. "Turbulence effects on supernova neutrinos". In: *Physical Review D* 82.12 (Dec. 2010), p. 123004. arXiv: 1006.0913.

[23] Eg Adelberger and a García. "Solar fusion cross sections. II. The pp chain and CNO cycles". In: *Reviews of Modern …* 83.March (2011). arXiv: arXiv:1004.2318v3.

[24] Ondřej Pejcha and Todd A. Thompson. "THE PHYSICS OF THE NEUTRINO MECHANISM OF CORE-COLLAPSE SUPERNOVAE". In: *The Astrophysical Journal* 746.1 (Feb. 2012), p. 106. arXiv: 1103.4864.

[25] James P. Kneller, Gail C. McLaughlin, and Kelly M. Patton. "Stimulated neutrino transformation with sinusoidal density profiles". In: *Journal of Physics G: Nuclear and Particle Physics* 40.5 (May 2013), p. 055002. arXiv: arXiv:1202.0776v1.

[26] Georg Raffelt, Srdjan Sarikas, and David De Sousa Seixas. "Axial Symmetry Breaking in Self-Induced Flavor Conversionof Supernova Neutrino Fluxes". In: *Physical Review Letters* 111.9 (Aug. 2013), p. 091101.

[27] a Malkus, A Friedland, and G. C. McLaughlin. "Matter-Neutrino Resonance Above Merging Compact Objects". In: 1 (Mar. 2014), pp. 1–6. arXiv: 1403.5797.

[28] Gianpiero Mangano, Alessandro Mirizzi, and Ninetta Saviano. "Damping the neutrino flavor pendulum by breaking homogeneity". In: *Physical Review D* 89.7 (Apr. 2014), p. 073017. arXiv: 1403.1892.

[29] Kelly M. Patton, James P. Kneller, and Gail C. McLaughlin. "Stimulated neutrino transformation through turbulence". In: *Physical Review D* 89.7 (Apr. 2014), p. 073022. arXiv: arXiv:1407.7835v1.

[30] Sean M. Couch and Christian D. Ott. "The Role of Turbulence in Neutrino-driven Core-collapse Supernova Explosions". In: *The Astrophysical Journal* 799.1 (Jan. 2015), p. 5.

[31] B. Muller and H.- T. Janka. "Non-radial instabilities and progenitor asphericities in core-collapse supernovae". In: *Monthly Notices of the Royal Astronomical Society* 448.3 (Feb. 2015), pp. 2141–2174.

[32] D. Vaananen and G. C. McLaughlin. "Uncovering the Matter-Neutrino Resonance". In: (Oct. 2015), pp. 1–16. arXiv: 1510.00751.

[33] Sovan Chakraborty et al. "Self-induced neutrino flavor conversion without flavor mixing". In: *Journal of Cosmology and Astroparticle Physics* 2016.03 (Mar. 2016), pp. 042–042. arXiv: 1602.00698.

[34] Hans-Thomas Janka, Tobias Melson, and Alexander Summa. "Physics of Core-Collapse Supernovae in Three Dimensions: A Sneak Preview". In: *Annual Review of Nuclear and Particle Science* 66.1 (2016), pp. 341–375. arXiv: 1602.05576.

[35] C. Patrignani et al. "Review of Particle Physics". In: *Chin. Phys.* C40.10 (2016), p. 100001.

[36] R. F. Sawyer. "Neutrino Cloud Instabilities Just above the Neutrino Sphere of a Supernova". In: *Physical Review Letters* 116.8 (2016), pp. 1–5. arXiv: 1509.03323.

[37] Meng-Ru Wu, Huaiyu Duan, and Yong-Zhong Qian. "Physics of neutrino flavor transformation through resonances". In: *Physics Letters B* 752 (Jan. 2016), pp. 89–94. arXiv: 1509.08975.

[38] Basudeb Dasgupta, Alessandro Mirizzi, and Manibrata Sen. "Fast neutrino flavor conversions near the supernova core with realistic flavor-dependent angular distributions". In: *Journal of Cosmology and Astroparticle Physics* 2017.02 (Feb. 2017), pp. 019–019. arXiv: 1609.00528.

[39] Ignacio Izaguirre, Georg Raffelt, and Irene Tamborra. "Fast Pairwise Conversion of Supernova Neutrinos: A Dispersion Relation Approach". In: *Physical Review Letters* 118.2 (Jan. 2017), p. 021101. arXiv: 1610.01612.

[40] Hans-Thomas Janka. *Neutrino Emission from Supernovae*. Ed. by Athem W. Alsabti and Paul Murdin. Cham: Springer International Publishing, 2017, pp. 1575–1604. ISBN: 978-3-319-21846-5.

[41] E. Kemp. "The Deep Underground Neutrino Experiment: The precision era of neutrino physics". In: *Astronomische Nachrichten* 338.9-10 (2017), pp. 993–999.

[42] *The Garching Core-Collapse Supernova Archive, http://wwwmpa.mpa-garching.mpg.de/ccsna*